Journal of Computational Physics 491 (2023) 112344

Contents lists available at ScienceDirect

Journal of Computational Physics

journal homepage: www.elsevier.com/locate/jcp

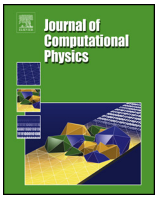

DeepStSNet: Reconstructing the quantum state-resolved thermochemical nonequilibrium flowfield using deep neural operator learning with scarce data

Jiaqi Lv [a,b], Qizhen Hong [a,*], Xiaoyong Wang [a], Zhiping Mao [c,*], Quanhua Sun [a,b]

[a] *State Key Laboratory of High Temperature Gas Dynamics, Institute of Mechanics, Chinese Academy of Sciences, 100190, Beijing, China*
[b] *School of Engineering Science, University of Chinese Academy of Sciences, Beijing, 100049, China*
[c] *School of Mathematical Sciences, Fujian Provincial Key Laboratory of Mathematical Modeling and High-Performance Scientific Computing, Xiamen University, Xiamen, 361005, China*

ARTICLE INFO

Article history:
Received 19 March 2023
Accepted 30 June 2023
Available online 17 July 2023

Keywords:
Hypersonic
Thermochemical nonequilibrium
State-to-state approach
Deep learning
Multiphysics
Data assimilation

ABSTRACT

The hypersonic flow is in a thermochemical nonequilibrium state due to the high-temperature caused by the strong shock compression. In a thermochemical nonequilibrium flow, the distribution of molecular internal energy levels strongly deviates from the equilibrium distribution (i.e., the Boltzmann distribution). It is intractable to directly obtain the microscopic nonequilibrium distribution from existed experimental measurements usually described by macroscopic field variables such as temperature or velocity. Motivated by the idea of deep multi-scale multi-physics neural network (DeepMMNet) proposed in [1], we develop in this paper a data assimilation framework called *DeepStSNet* to accurately reconstruct the quantum state-resolved thermochemical nonequilibrium flowfield by using *sparse experimental measurements* of vibrational temperature and pre-trained deep neural operator networks (DeepONets). In particular, we first construct several DeepONets to express the coupled dynamics between field variables in the thermochemical nonequilibrium flow and to approximate the state-to-state (StS) approach, which traces the variation of each vibrational level of molecule accurately. These proposed DeepONets are then trained by using the numerical simulation data, and would later be served as building blocks for the DeepStSNet. We demonstrate the effectiveness and accuracy of DeepONets with different test cases showing that the density and energy of vibrational groups as well as the temperature and velocity fields are predicted with high accuracy. We then extend the architectures of DeepMMNet by considering a simplified thermochemical nonequilibrium model, i.e., the 2T model, showing that the entire thermochemical nonequilibrium flowfield is well predicted by using scattered measurements of full or even partial field variables. We next consider a more accurate and complex thermochemical nonequilibrium model, i.e., the StS-CGM model, and develop a DeepStSNet for this model. In this case, we employ the coarse-grained method, which divides the vibrational levels into groups (vibrational bins), to alleviate the computational cost for the StS approach in order to achieve a fast but reliable prediction with DeepStSNet. We test the present DeepStSNet framework with sparse numerical simulation data showing that the predictions are in excellent agreement with the reference data for test cases. We further employ the DeepStSNet to assimilate a few experimental measurements of vibrational temperature

---

[*] Corresponding authors.
E-mail addresses: lvjiaqi@imech.ac.cn (J. Lv), hongqizhen@imech.ac.cn (Q. Hong), wangxy@imech.ac.cn (X. Wang), zpmao@xmu.edu.cn (Z. Mao), qsun@imech.ac.cn (Q. Sun).

https://doi.org/10.1016/j.jcp.2023.112344
0021-9991/© 2023 Elsevier Inc. All rights reserved.

obtained from the shock tube experiment, and the detailed non-Boltzmann vibrational distribution of molecule oxygen is reconstructed by using the sparse experimental data for the first time. Moreover, by considering the inevitable uncertainty in the experimental data, an average strategy in the predicting procedure is proposed to obtain the most probable predicted fields. The present DeepStSNet is general and robust, and can be applied to build a bridge from sparse measurements of macroscopic field variables to a microscopic quantum state-resolved flowfield. This kind of reconstruction is beneficial for exploiting the experimental measurements and uncovering the hidden physicochemical processes in hypersonic flows.

© 2023 Elsevier Inc. All rights reserved.

1. Introduction

Hypersonic re-entry and hypersonic cruise would result in a strong bow shock at the front of a vehicle. The high temperature, due to the compression of the shock wave, inside the shock layer gives rise to thermochemical nonequilibrium phenomena such as relaxation between different internal energy modes, dissociation, ionization, and radiation. All these processes occur at finite-rate [2], and their characteristic times are usually comparable to the characteristic time of the gas flow. The aforementioned physical processes are strongly coupled with fluid dynamics and significantly affect the vehicle's thermal environment and aerodynamic performance. Therefore, accurately modeling the thermochemical nonequilibrium flows is a key point to developing hypersonic flight technology.

Great efforts have been devoted to developing accurate physical models for hypersonic thermochemical nonequilibrium flows. The two-temperature (2T) model [3] has been proposed as the primary tool to describe thermochemical nonequilibrium flows and is widely used in engineering. In the 2T model, the population of each internal energy mode is assumed to follow a Boltzmann distribution under a particular temperature, namely, the translational and rotational energy modes are described by temperature T_{tr}, and the vibrational (and electronic) energy is treated by temperature T_v. Besides the well-known Park model [4], the coupled vibration-dissociation-vibration (CVDV) model [5] with preferential dissociation of high vibrational levels and the Macheret-Fridman (MF) model [6] that introduces two dissociation mechanisms, among others, are developed to better consider the vibration-dissociation coupling. Moreover, the effect of non-Boltzmann internal energy distribution on chemical kinetics has been considered recently by introducing the non-Boltzmann correction into the 2T models [7,8]. However, there are empirical parameters in the above physical models and corrections. Consequently, these models cannot accurately capture the nonequilibrium (non-Boltzmann) distribution of internal energy levels. Therefore, the accuracy of the above models in describing a strong thermochemical nonequilibrium flow deviates case by case.

The rapid development of computational resources has promoted to use the high-fidelity state-to-state (StS) approach [9] in the simulation of thermochemical nonequilibrium flows [9–15]. The StS approach treats each internal energy level as a pseudo-specie in the gas mixture by solving the master equations, and thereby the non-Boltzmann distribution of internal energy mode can be represented. Transition processes between the internal energy levels of molecules and state-specific chemical reactions are considered elementary reactions in the StS kinetics. Therefore, the key for the StS approach is to get the state-specific reaction rate coefficients for the state transitions and chemical reactions, which are mostly taken from the data calculated by the Forced Harmonic Oscillator model [16,17], Quasi-Classical Trajectory calculation [12,18,19] and even mixed Quantum-Classical calculation [20,21] for the common neutral air species ($\mathrm{N_2, O_2, NO, N, O}$). Since a typical StS simulation needs to calculate a large number of internal energy levels and state-to-state transitions, it is very time-consuming and so far mostly limited to simple one-dimensional geometries such as post-shock flows [10,13,22,23], nozzle flows [24,25] and flows along the stagnation streamline [14]. Although the recent use of GPU allows one to apply the StS approach with reduced StS kinetics to calculate two-dimensional configurations [15], applying the StS approach to realistic engineering problems is still intractable. To reduce the considerable computational cost, the coarse-grained method (CGM) [11,12,26] has been developed for the StS approach (called StS-CGM hereafter), in which the internal energy levels are lumped into different groups, thus less number of the master equations (for groups) and transitions (between groups) remain. The population of the internal energy levels is then reconstructed (assuming a piecewise distribution) from groups by the maximum entropy principle [27]. Different level reconstruction assumptions concerning the specification of the group distribution have been studied in [26].

In the experimental study of thermochemical nonequilibrium flow, it is intractable to directly obtain the detailed molecular energy level distribution from experimental measurements or flight data, which are usually limited to macroscopic field variables like temperature or velocity [28,29]. Therefore, the main motivation of the present work is to integrate the results of StS calculations with *scarce experimental data* to infer the detailed population of internal energy levels in the experimental flowfield. Assimilating scarce experimental data is non-trivial because, in the conventional approaches, it relies on repeated procedures with solutions of governing equations, and knowledge from previous assimilation tasks is usually not effectively exploited. Now data-driven and data assimilation via *machine learning* are used successfully in many scenarios, for example, discovering the macroscopic governing equations in fluid mechanics [30] and unknown equations hidden in the sufficient data [31], inverse problems in supersonic flows [32], to name but a few. Recently a new data assimilation framework, i.e., the deep multi-scale multi-physics neural network (DeepMMNet) [1,33], has been demonstrated to assimilate scarce data from sensors accurately and efficiently with the help of pre-trained deep neural operator networks (DeepONets), which are used to approximate continuous nonlinear functional or operator [34,35] and proposed by Lu et al. in [36]. More precisely, DeepMMNets use neural networks as surrogate models and integrate several pre-trained DeepONets [36] with a few measurements to produce the entire fields of the coupled multi-physics and multi-scale systems [1,33]. The DeepONet has been successfully employed to several problems such as electroconvection multiphysics fields [33], prediction of linear instability waves in high-speed boundary layers [37], modeling of the inelastic reaction rates [38], etc. In [1], both parallel and series DeepMMNets have been proposed for hypersonic flows with finite-rate chemistry. These two architectures of DeepMMNet have been demonstrated to successfully infer the set of all fields in the domain of interest with scarce sensor data.

However, the thermochemical nonequilibrium effect, which is the most significant feature of hypersonic flows, has not been considered in the previous work [1]. Therefore, the aim in this paper is to extend the idea of DeepMMNet to develop a data assimilation framework, based on the state-to-state approach with the coarse-grained method, for solving the thermochemical nonequilibrium flows and reconstructing the vibrational state-resolved flowfield at the condition of sparse experimental measurements (specifically, the measured vibrational temperatures in the experiment of Ibraguimova et al. [28]). The present framework, named DeepStSNet hereafter, will use the pre-trained DeepONets for StS-CGM field variables as building blocks.

The rest of the paper is organized as follows: in Sec. 2, we first introduce the StS approach for simulating the postshock thermochemical nonequilibrium flows of O_2/O gas mixture. Then we present the architecture of DeepONet and the data generation procedure. In Sec. 3, we extend the DeepMMNet framework to develop and test a data assimilation framework for the reduced 2T model. In Sec. 4, we design and test the architecture of DeepStSNet based on the StS-CGM model. The related DeepONets for StS-CGM field variables are also developed and tested. In Sec. 5, the DeepStSNet is then employed to assimilate a few experimental measurements of vibrational temperature in the shock tube experiment and, to infer the full fields. The molecule's detailed non-Boltzmann vibrational energy distribution is reconstructed from scarce experimental data for the first time. Concluding remarks are given in the last section.

2. Methodology and data generation

Ibraguimova et al. [28] measured vibrational temperature T_v behind normal shock wave at temperatures 4000-10800 K in undiluted oxygen by studying oxygen absorbance in the Schumann-Runge band. These experimental measurements will serve as input data of DeepStSNet training (see the details in Sec. 5), so we first make StS simulations for the postshock flows with different freestream conditions of O_2/O gas mixture and generate the reference dataset. Since the number of collisions to reach equilibrium for vibration is larger than the one for rotation [39], the rotational energy mode of O_2 is assumed to be in equilibrium with the translational energy mode, corresponding to a translational-rotational temperature T_{tr} (called T in short hereafter). Moreover, only the ground electronic state is considered for O_2 and O, which is a good approximation in the temperature range of interest. Therefore, the present paper only applies the StS approach to the vibrational energy mode.

In this section, we first introduce governing equations for the StS approach and the related physics. Then we present the architecture of DeepONet, and describe the data generation process and the details of the test samples.

2.1. Governing equations and physical models

The StS approach well describes the thermochemical nonequilibrium processes by treating each internal energy level as a pseudo-species. Therefore, there is no need to make assumptions on the formulation of the internal energy level distribution. A total of 46 vibrational levels proposed in [40] are considered for molecular oxygen O_2 in its ground electronic state. The postshock flow of O_2/O mixture is governed by the following one-dimensional steady compressible Euler equations:

$$\frac{d}{dx}\begin{bmatrix}\rho_i u\\ \rho u^2\\ \rho u H\end{bmatrix}=\begin{bmatrix}\omega_i\\ -\frac{dp}{dx}\\ 0\end{bmatrix}, \tag{1}$$

where ρ_i is species density with $i = 0-45$ representing vibrational levels of O_2 and $i = 46$ representing O. ρ, u, p and H are the density, velocity, pressure and specific total enthalpy of the gas mixture, respectively, and x is the distance coordinate behind the normal shock. ω_i is the mass production rate of species i and obtained by the state-to-state kinetics in the master equations. Specifically,

$$\begin{aligned}\frac{N_{\mathrm{Av}}}{M_{\mathrm{O}_2}}\omega_{\mathrm{O}_2(i)} = & \sum_j \sum_l \sum_m k_{\mathrm{V-V-T}}(l,m \to i,j) n_{\mathrm{O}_2(l)} n_{\mathrm{O}_2(m)} \\ & - \sum_j \sum_l \sum_m k_{\mathrm{V-V-T}}(i,j \to l,m) n_{\mathrm{O}_2(i)} n_{\mathrm{O}_2(j)} \\ & + \sum_j \left[k_{\mathrm{V-T}}(j \to i) n_{\mathrm{O}_2(j)} n_{\mathrm{O}} - k_{\mathrm{V-T}}(i \to j) n_{\mathrm{O}_2(i)} n_{\mathrm{O}} \right] \\ & + k^{\mathrm{M}}_{\mathrm{V-D}}(c \to i) n_{\mathrm{O}}^2 n_{\mathrm{M}} - k^{\mathrm{M}}_{\mathrm{V-D}}(i \to c) n_{\mathrm{O}_2(i)} n_{\mathrm{M}}\end{aligned}, \tag{2}$$

where N_{Av} is the Avogadro constant, M_{O_2} is the molecular mass of O_2 and n_i is the species number density. $k_{\mathrm{V-V-T}}(i, j \to l, m)$ are the vibration-vibration-translation (V-V-T) transition rate coefficients of the processes

$$\mathrm{O}_2(i) + \mathrm{O}_2(j) \leftrightarrow \mathrm{O}_2(l) + \mathrm{O}_2(m). \tag{3}$$

These state-specific rate coefficients are obtained based on the forced harmonic oscillator model by Hao et al. [10] and validated against the mixed Quantum-Classical calculations [41] by Gu et al. [23].

$k_{\mathrm{V-T}}(i \to j)$ are the vibration-translation (V-T) transition rate coefficients of the processes

$$\mathrm{O}_2(i) + \mathrm{O} \leftrightarrow \mathrm{O}_2(j) + \mathrm{O}. \tag{4}$$

These rate coefficients are obtained from the quasi-classical trajectory calculations by Esposito et al. [42].

Furthermore, $k^{\mathrm{M}}_{\mathrm{V-D}}(i \to c)$ are the vibration-dissociation (V-D) bound-free transition rate coefficients of the processes

$$\mathrm{O}_2(i) + \mathrm{M} \leftrightarrow \mathrm{O} + \mathrm{O} + \mathrm{M}. \tag{5}$$

The V-D rate coefficients of $\mathrm{O}_2 - \mathrm{O}$ collision are obtained from the quasi-classical trajectory calculations by Esposito et al. [42], while the V-D data reported in the Stellar database [43] are adopted for $\mathrm{O}_2 - \mathrm{O}_2$ collision.

The above processes make up the state-to-state kinetics considered in the present StS calculation for O_2/O mixture. The backward rate coefficients of the above processes are derived from the detailed balance principle.

The post-shock vibrational distribution function (VDF) of O_2 can be obtained by solving Eqs. (1), so one can trace the detailed evolution of the vibrational energy levels. However, the above StS calculation is time-expensive, thence various vibration-dissociation coupling models based on the two-temperature (2T) assumption have been developed [3,5,6] to reduce the computational cost. The two-temperature assumption assumes that the translational and rotational energy modes are described by temperature T_{tr}, the vibrational energy mode is treated by temperature T_v, and the population of each internal energy mode follows a Boltzmann distribution. Therefore, the postshock flow of O_2/O mixture based on the reduced 2T model is governed by the following one-dimensional steady compressible Euler equations:

$$\frac{d}{dx}\begin{bmatrix} \rho_s u \\ \rho u^2 \\ \rho u H \\ \rho u e_v \end{bmatrix} = \begin{bmatrix} \omega_s \\ -\frac{dp}{dx} \\ 0 \\ \omega_v \end{bmatrix}, \tag{6}$$

where ρ_s and ω_s are the density and the mass production rate of the species s, i.e., O_2 or O. It is noted that an additional vibrational energy conservation equation is added in the above equations, and e_v is vibrational energy per unit mass of the gas mixture. The VDF of O_2 is reconstructed by Boltzmann distribution from T_v (obtained from e_v), so it is no longer needed to solve the master equations as in the StS approach. Moreover, ω_v is the source term of vibrational energy, and it consists of two parts: $\omega_{\mathrm{V-T}}$ and $\omega_{\mathrm{V-D}}$. $\omega_{\mathrm{V-T}}$ is the energy transfer between the translational-rotational and vibrational modes and is usually modeled using the Landau-Teller model [44]. $\omega_{\mathrm{V-D}}$ is the vibrational energy added or removed by reactions, whose formulation varies with the 2T models such as preferential and non-preferential models [3,5,6,8].

The reduced 2T model is more efficient than the StS approach but less accurate due to the simplified physical assumptions and existing empirical parameters. Eqs. (6) are not explicitly solved in the present paper, and the field variables in the 2T framework are extracted from the StS results, which will be described in Sec. 2.3.

2.2. DeepONet architecture

The universal approximation theorem states that a neural network can not only approximate a continuous function, but also nonlinear continuous operators [35]. Lu et al. [36] proposed deep operator networks (DeepONets) to learn nonlinear operators from data based on the universal approximation theorem. The DeepONet, whose architecture is shown in Fig. 1, consists of a branch network that takes the function $u(x)$ as the input and a trunk network that takes the location points y_i as the input, learning the mapping $G : (u, y) \to G(u)(y) = \sum_{i=1}^{p} b_i t_i$, where $b_i, i = 1, 2, \ldots, p$ and $t_i, i = 1, 2, \ldots, p$ are the outputs of the branch net and trunk net, respectively.

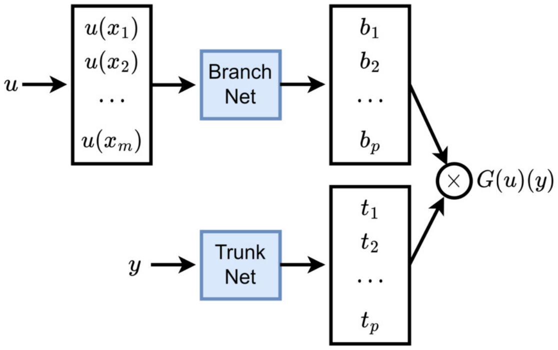

Fig. 1. Schematic of the unstacked DeepONet [36], which is the building block of the DeepMMNet [1] and DeepStSNet. DeepONet learns the mapping from the function u to $G(u)$.

Table 1
Freestream conditions used in the StS calculations.

M_∞	Pressure	Temperature
10-15	106.658 Pa	295 K

DeepONet uses the weakest possible constraints on the dataset, and networks such as the convolutional neural network can be implemented depending on the problem. It is important to note that we train the DeepONet offline and make predictions online without further training in the present work. We develop DeepONets in Sec. 3.1 for the 2T model and in Sec. 4.2 for the StS-CGM model, respectively, to express the coupled dynamics between these field variables. By inputting some field variables, the DeepONets can accurately predict all the remaining fields. Furthermore, as a substitute for directly solving the governing equations, DeepONets will be used as building blocks for the DeepMMNet proposed in Sec. 3 and DeepStSNet proposed in Sec. 4.

2.3. Data generation

We describe in this subsection the process for generating the reference dataset. Since we aim to assimilate the experiments reported in [28], the postshock flows of O_2/O gas mixture are calculated by the StS approach. The selected freestream conditions are given in Table 1. Specifically, the freestream pressure and temperature are the same as the ones in the highest total enthalpy case of the experiments [28], and the freestream gas is pure O_2. Furthermore, the freestream Mach number (M_∞) is varied within the range of [10-15], which contains the experimental Mach number.

The post-shock values (or the inflow conditions for StS calculation) are derived from Rankine-Hugoniot relations, assuming that vibrational modes and gas composition are frozen across the shock wave. The stiff Eqs. (1) are solved by the CVODE solver [45], and field variables U, T, $\rho_{O_2(i)}$ and ρ_O (these variables are called ‘StS variables’ hereafter) behind the normal shock are obtained. The simulations are performed on a uniform grid of 1000 nodes covering 5 mm in the distance behind the normal shock. Totally, the dataset contains 501 cases as the freestream Mach number step is 0.01. And we randomly choose 425 of them for the training set, 50 for the validation set, and 26 for the test set in developing DeepONets in Secs. 3.1 and 4.2.

Although Eqs. (6) for the 2T model are not explicitly solved in the present paper, the field variables in the 2T framework can be extracted from the above StS results. Specifically, a vibrational temperature is extracted from the VDF of O_2 as follows:

$$T_\mathrm{v} = \frac{\varepsilon_1 - \varepsilon_0}{k_B \ln\left[n_{O_2(1)}/n_{O_2(0)}\right]}, \tag{7}$$

where ε_i is the vibrational energy and k_B is the Boltzmann constant. Note that the above definition is also called the vibrational temperature of the first excited state. Moreover, the density of O_2, namely ρ_{O_2}, is obtained by summing the densities of all the vibrational levels $\rho_{O_2(i)}$. In the end, field variables U, T, T_v, ρ_{O_2} and ρ_O (these variables are called ‘2T variables’ hereafter) behind the normal shock are obtained.

3. DeepMMNet for the 2T model

We begin by constructing DeepMMNets for the 2T model in describing thermochemical nonequilibrium flow. To this end, we develop DeepONets for learning the coupled dynamics between 2T variables. Then these pre-trained DeepONets are used as the building blocks for the DeepMMNets. This extension helps to assimilate the scarce sensor data to infer the set of all field variables representing the thermochemical nonequilibrium feature in hypersonic flows. Note that this kind of

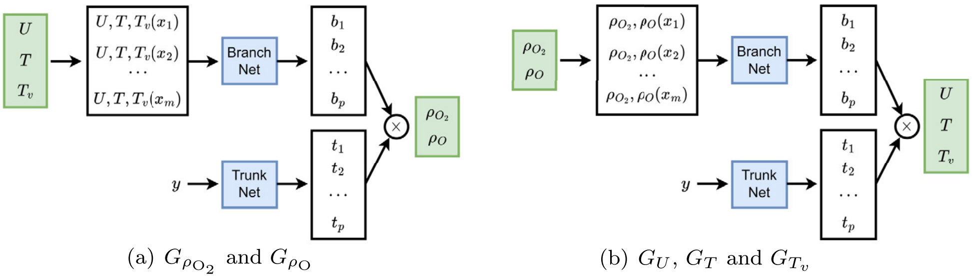

(a) $G_{\rho_{O_2}}$ and G_{ρ_O}

(b) G_U, G_T and G_{T_v}

Fig. 2. Schematic of DeepONets for the coupled dynamics between the 2T variables. (a) DeepONets $G_{\rho_{O_2}}$ and G_{ρ_O}. (b) DeepONets G_U, G_T and G_{T_v}.

reconstruction reported in this section is based on the two-temperature assumption, so the VDF of O_2 is reconstructed by the Boltzmann distribution from T_v.

3.1. DeepONets for the coupled dynamics between 2T variables

We now develop DeepONets for learning nonlinear operators (namely approximating Eqs. (6)) to represent the coupled dynamics between the flow and the chemical species. As mentioned in Sec. 2.2, the present DeepONet has two sub-networks: a trunk network takes the coordinates y of the output function, and a branch network takes the discretized input function at the sensors $\{x_1, x_2, \ldots, x_{100}\}$. For convenience, the number and values of y are the same as the sensor points in the present work.

We then design five independent DeepONets describing the coupled dynamics between the flow and the chemical species as follows:

(i) DeepONets $G_{\rho_{O_2}}$ and G_{ρ_O} taking the field variables $[U, T, T_v]$ as the inputs for the branch net and the chemical species $\left[\rho_{O_2}, \rho_O\right]$ as the outputs (see Fig. 2(a)).
(ii) DeepONets G_U, G_T and G_{T_v} taking the chemical species $\left[\rho_{O_2}, \rho_O\right]$ as the inputs for the branch net and field variables $[U, T, T_v]$ as the outputs (see Fig. 2(b)).

We take the densities of O_2 and O in the logscale to improve the accuracy and robustness in the DeepONets training, while we use the non-dimensionalized field variables U, T and T_v. The DeepONets are trained independently by minimizing the mean squared error (MSE) loss function. As mentioned in Sec. 2.3, the StS dataset is divided into a training, a validation, and a test dataset according to the ratio of 0.85: 0.1: 0.05. All the above DeepONets have the same hyperparameters listed in Appendix A. We have performed sensitivity tests with different training parameters, and the results are similar to the ones obtained by the reported parameters.

We show the comparisons between the predictions of DeepONets and the reference data in Fig. 3. It is observed that each DeepONet of G_U, G_T, G_{T_v}, $G_{\rho_{O_2}}$ and G_{ρ_O} prediction, randomly chosen from cases in the test dataset with different freestream Mach number, is in excellent agreement with the reference data obtained in Sec. 2.3. It is noted that the density of O varies by orders of magnitude (zero at post-shock position) downstream of the shock, and the DeepONet G_{ρ_O} predicts the variation accurately. The corresponding loss functions for training and validation datasets on G_U, G_T and G_{T_v} are also shown in Fig. 3, and the trends and orders of magnitude of the loss functions of the density variables are similar. The validation losses are commensurate with the training losses. The perfect agreement between prediction and reference data demonstrates that the present DeepONets have been trained successfully to represent the coupled dynamics between 2T variables, and they cost much less than directly solving the governing equations for obtaining flow parameters. These pre-trained DeepONets will serve as building blocks for the design of DeepMMNet for the 2T model.

3.2. Parallel DeepMMNet for the 2T model

In practical applications, measurement data in the thermochemical nonequilibrium flow are only available for some field variables, and the number of sensors is usually sparse. However, the above DeepONets require full knowledge of input functions to make predictions. Mao et al. [1] relax the above requirement by proposing the data assimilation framework, DeepMMNet, to infer the full fields when only a few measurements (sensor data) for some field variables are available. The pre-trained DeepONets are embedded in the DeepMMNet framework as the physics constraints. However, the thermochemical nonequilibrium effects have yet to be considered in the previous work of Mao et al. [1]. Therefore, we extend the DeepMMNet framework for the 2T model in the following.

We start with the parallel DeepMMNet architecture for the 2T model (see Fig. 4 for the schematic), which supposes sparse sensor data for all the 2T variables are needed. For convenience, the measurements of these variables share the same space coordinates in the following test examples, i.e., $\rho^j_{O_2,data}$, $\rho^j_{O,data}$, U^j_{data}, T^j_{data} and $T^j_{v,data}$, $j = 1, 2, \ldots, n_d$, and n_d is

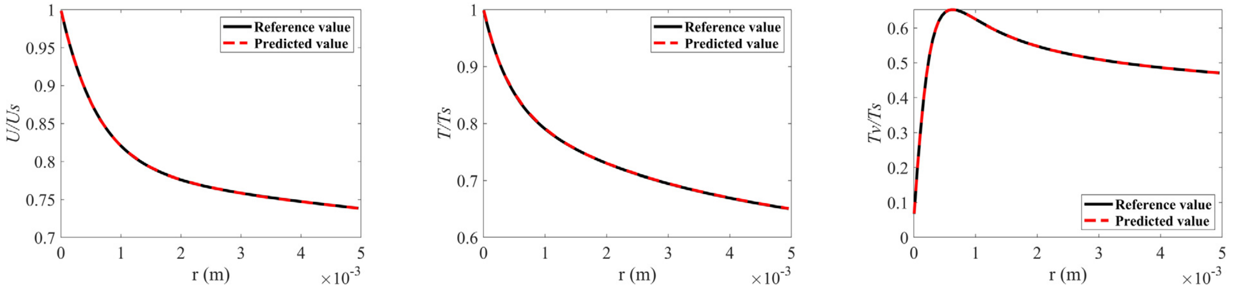

(a) U for $M_\infty = 10.44$ (b) T for $M_\infty = 11.38$ (c) T_v for $M_\infty = 13.08$

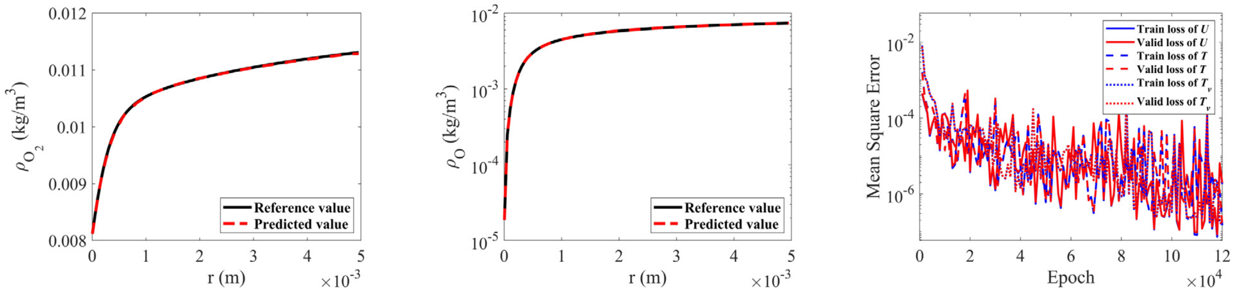

(d) ρ_{O_2} for $M_\infty = 12.48$ (e) ρ_O for $M_\infty = 14.71$ (f) Losses for U, T, T_v

Fig. 3. (a-e) Predictions of DeepONets for the 2T model, and (f) the training and validation losses for DeepONets G_U, G_T and G_{T_v}.

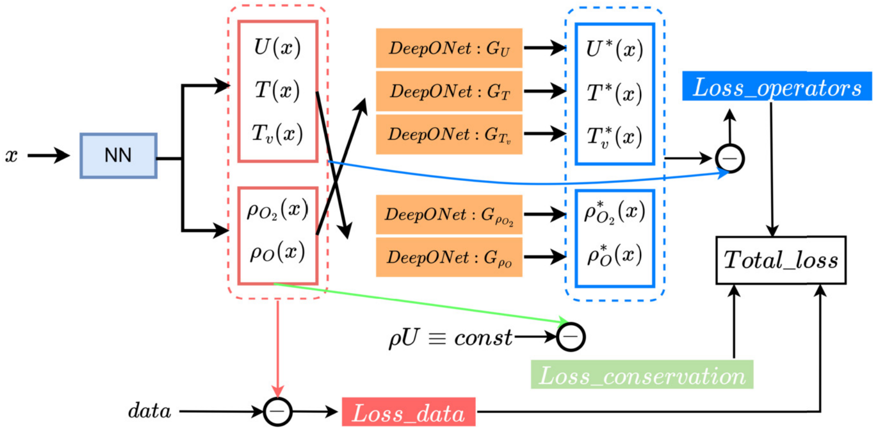

Fig. 4. Schematic of the parallel DeepMMNet. Sparse sensor data for all the 2T variables are needed in this parallel framework.

the number of measurements data. A simple neural network (NN) is trained, which takes the coordinate x as input and all the 2T field variables as the outputs. Then the field variables U, T, T_v are fed to independent pre-trained DeepONets $G_{\rho_{O_2}}$ and G_{ρ_O}, and the predicted field variables ${\rho_{O_2}}^*$ and ${\rho_O}^*$ are obtained, respectively. Similarly, field variables ρ_{O_2} and ρ_O are fed to independent pre-trained DeepONets G_U, G_T, G_{T_v}, and the predicted field variables U^*, T^*, T_v^* are obtained, respectively. Furthermore, an additional restriction related to the global mass conservation (i.e., $\rho(x)U(x) \equiv Const$ derived from the continuity equation in the present one-dimensional post-shock flow) is added in the framework to make the prediction more robustly and physically. Finally, the total loss is obtained by summing the following terms:

$$\mathcal{L} = w_{data}\frac{\mathcal{L}_{\text{data}}}{n_d} + w_{op}\frac{\mathcal{L}_{op}}{n_{op}} + w_{reg}\mathcal{L}_{\text{reg}} + w_G\frac{\mathcal{L}_G}{n_G}, \tag{8}$$

in which data loss $\mathcal{L}_{data}$ represents the mean square errors (MSE) between the NN outputs and the reference data, i.e.,

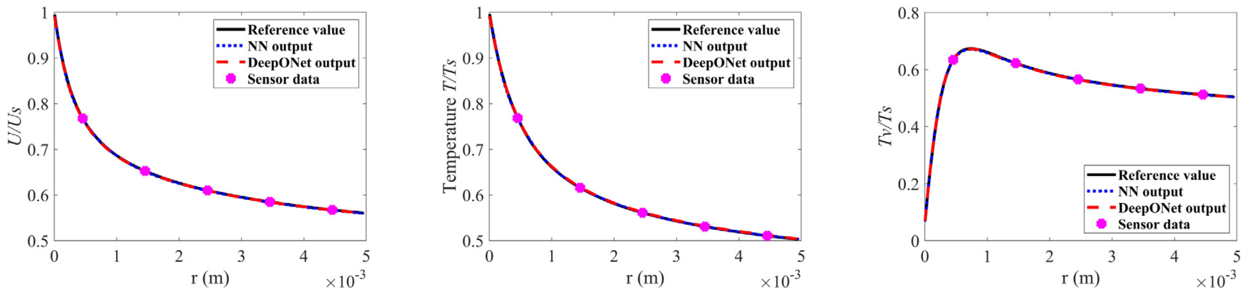

(a) Variable U (b) Variable T (c) Variable T_v

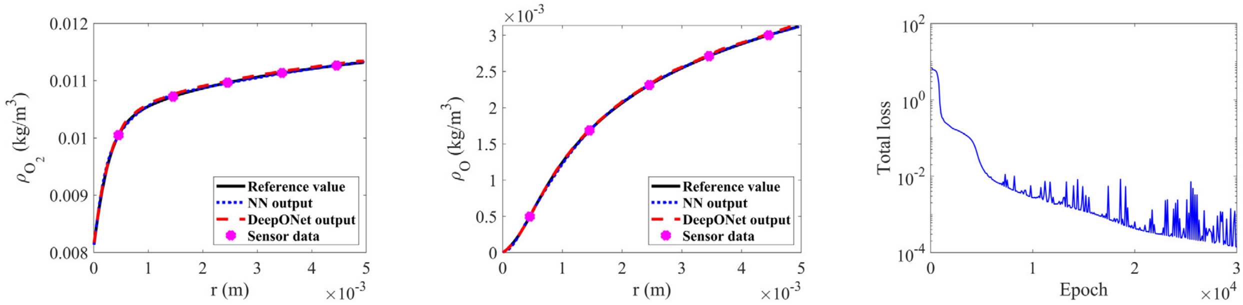

(d) Variable ρ_{O_2} (e) Variable ρ_O (f) Training loss

Fig. 5. Predictions of the parallel DeepMMNet for the 2T model in the test case with $M_\infty = 12.71$. The pink circle symbols represent sensor data extracted from the StS calculations (labeled as 'Reference value' in the figure). (For interpretation of the colors in the figure(s), the reader is referred to the web version of this article.)

$$\begin{aligned}\mathcal{L}_{\text{data}} =& \sum_{j=1}^{n_d}\sum_{k\in\{O_2,O\}}\left\|\rho^j_{k,\text{ data}} - \rho_k\left(x_j\right)\right\|^2 + \sum_{j=1}^{n_d}\left\|U^j_{\text{data}} - U\left(x_j\right)\right\|^2 \\ &+ \sum_{j=1}^{n_d}\left\|T^j_{\text{data}} - T\left(x_j\right)\right\|^2 + \sum_{j=1}^{n_d}\left\|T^j_{v_{\text{data}}} - T_v\left(x_j\right)\right\|^2 .\end{aligned} \tag{9}$$

The operator loss $\mathcal{L}_{op}$ is the MSE between the NN outputs and the DeepONets predictions, i.e.,

$$\begin{aligned}\mathcal{L}_{op} =& \sum_{j=1}^{n_{op}}\sum_{k\in\{O_2,O\}}\left\|\rho^*_k\left(x_j\right) - \rho_k\left(x_j\right)\right\|^2 + \sum_{j=1}^{n_{op}}\left\|U^*\left(x_j\right) - U\left(x_j\right)\right\|^2 \\ &+ \sum_{j=1}^{n_{op}}\left\|T^*\left(x_j\right) - T\left(x_j\right)\right\|^2 + \sum_{j=1}^{n_{op}}\left\|T^*_v\left(x_j\right) - T_v\left(x_j\right)\right\|^2 ,\end{aligned} \tag{10}$$

where n_{op} is the number of points for field variables. The global mass conservation loss $\mathcal{L}_G$ gives the MSE between the mass fluxes of the NN outputs and the reference data, i.e.,

$$\mathcal{L}_G = \sum_{j=1}^{n_G}\left\|\rho\left(x_j\right)U\left(x_j\right) - \text{ Const }\right\|^2, \tag{11}$$

where $\rho(x) = \rho_{O_2}(x) + \rho_O(x)$, n_G is the number of points for the global mass conservation and the value 'Const' takes from the average of the known data Const $= \frac{1}{n_d}\sum_{j=1}^{n_d}\rho^j_{data}U^j_{data}$.

Moreover, the L_2 regularization of the training parameters (i.e., $\mathcal{L}_{\text{reg}} = \|\theta\|_2^2$, θ is the set of training parameters of the neural network) is also added in Eq. (8) to avoid overfitting and stabilize the training process. The parameters w_{data}, w_{op}, w_G and w_{reg} in Eq. (8) are the weighting coefficients for each loss term.

To test the above parallel DeepMMNet framework for the 2T model, we randomly choose a test sample from the test dataset and assume five reference data are known for all the 2T variables, which means $n_d = 5, n_{op} = n_G = 100$. With many pre-tests, we set $w_{data} = w_{op} = w_G = 1.0$ for fast training, and it has only a minor influence on whether the regularization term is used or not. The hyperparameters for training the parallel DeepMMNet are listed in Appendix A.

It is observed in Fig. 5 that the outputs of both NN and DeepONets are available in training, and both of them are smooth and accurate (compared to the sparse input sensor data and reference values of the field), which is a result of adding $\mathcal{L}_{op}$

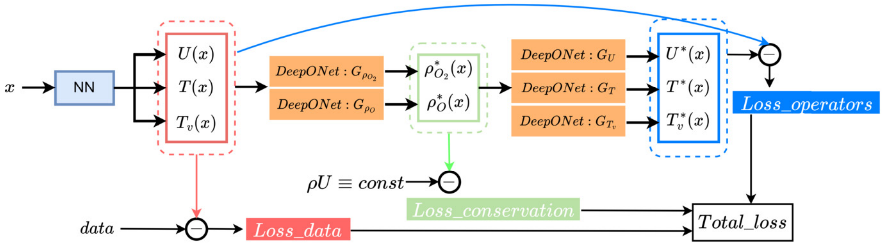

Fig. 6. Schematic of the series DeepMMNet. Sparse sensor data for variables U, T and T_v are needed in this series framework.

(a surrogate model for the governing equations [46]) and $\mathcal{L}_G$ (embedding the physical mass conservation constraint) in the total loss. In this test case, it is seen from Fig. 5 that the vibrational temperature first increases due to the V-T energy relaxation and decays after maximum value due to the vibration-dissociation coupling, and a considerable amount of O_2 is dissociated because of the high post-shock temperature.

Although the above parallel DeepMMNet performs well in inferring the entire thermochemical nonequilibrium flowfield (on the assumption of two-temperature), the training still requires sensor data of all the field variables. The above requirement is usually unpractical in the applications because some 2T variables are rather difficult to measure directly. In addition, the number of measurements is generally sparse. Therefore we extend the series DeepMMNet for the 2T model to address the above issues in the following.

3.3. Series DeepMMNet for the 2T model

In the practical use of data assimilation, only sparse data of some 2T variables, such as velocity and temperature, are expected to be available. Therefore, we extend the series DeepMMNet architecture [1] for the 2T model, which in the present case only requires a few data of the velocity U and temperatures T and T_v to predict all the remaining field variables. The series DeepMMNet architecture is adjusted from the parallel one and shown in Fig. 6. A simple NN is trained, which takes the coordinate x as input and only variables U, T and T_v as the outputs. The NN outputs U, T and T_v are then fed as the inputs to the pre-trained $G_{\rho_{O_2}}$ and G_{ρ_O} which outputs $\rho^*_{O_2}$ and ρ^*_O respectively. The densities $\rho^*_{O_2}$ and ρ^*_O are fed again to the pre-trained G_U, G_T and G_{T_v} that outputs variables U^*, T^* and T^*_v respectively. Note that the inputs to G_U, G_T and G_{Tv} are 'naturally' regularized because they are the outputs of the upstream DeepONets, and the physics modeled by these operators are encoded during their training. Moreover, an additional restriction related to global mass conservation (the mass flux is now calculated using ρ^* and U^*) is again added to the framework. Finally, the total loss is also represented by Eq. (8), and the loss terms are given as follows:

$$
\begin{aligned}
\mathcal{L}_{\text{data}} &= \sum_{j=1}^{n_d} \left\| U_{\text{data}}^j - U\left(x_j\right) \right\|^2 + \sum_{j=1}^{n_d} \left\| T_{\text{data}}^j - T\left(x_j\right) \right\|^2 + \sum_{j=1}^{n_d} \left\| T_v{}_{\text{data}}^j - T_v\left(x_j\right) \right\|^2, \\
\mathcal{L}_{op} &= \sum_{j=1}^{n_{op}} \left\| U^*\left(x_j\right) - U\left(x_j\right) \right\|^2 + \sum_{j=1}^{n_{op}} \left\| T^*\left(x_j\right) - T\left(x_j\right) \right\|^2 + \sum_{j=1}^{n_{op}} \left\| T_v{}^*\left(x_j\right) - T_v\left(x_j\right) \right\|^2, \\
\mathcal{L}_G &= \sum_{j=1}^{n_G} \left\| \rho^*\left(x_j\right) U^*\left(x_j\right) - \text{Const} \right\|^2.
\end{aligned}
\tag{12}
$$

To validate the series DeepMMNet architecture, a test sample is randomly selected from the test dataset and only 2 reference data points are known for variables U, T and T_v. Therefore, $n_d = 2, n_{op} = n_G = 100$. With a large number of pre-tests, we set $w_{data} = w_{op} = w_G = 1.0$ and $w_{reg} = 6 \times 10^{-5}$ for fast training. The hyperparameters for training the series DeepMMNet are listed in Appendix A.

Fig. 7 shows that the serial DeepMMNet results (NN and DeepONet outputs) agree well with the sensor data and reference values. Note that we do not use any sensor data of densities ρ_{O_2} and ρ_O in the neural network training, but we can still predict these variables accurately thanks to the pre-trained DeepONets. Moreover, it is found that the absolute value of the total loss increases with increasing weight w_{reg}, but the declining trend (though not shown in the figure) is smoother. The above results show that one can predict all field variables without complete knowledge of the fields by using the serial DeepMMNet, even with fewer sensor data of fewer variables.

To summarize, both the parallel and series DeepMMNets perform well in predicting the 2T variables and thermochemical nonequilibrium flowfield with sparse sensor data. They can incorporate newly added measurements for learning to achieve data assimilation. In addition, the pre-trained DeepONets and global mass conservation constraint implicitly describe the thermochemical nonequilibrium processes and contain the physics law of the hypersonic flow. The framework to predict the quantum state-resolved thermochemical nonequilibrium flowfield is developed in the next section.

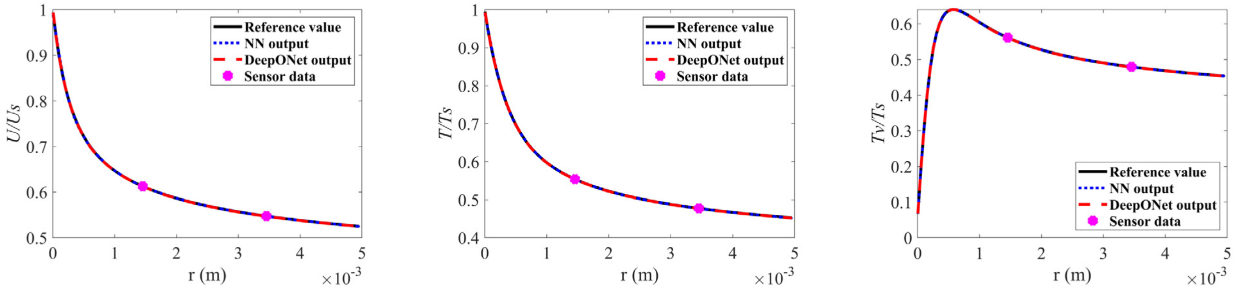

(a) Variable U (b) Variable T (c) Variable T_v

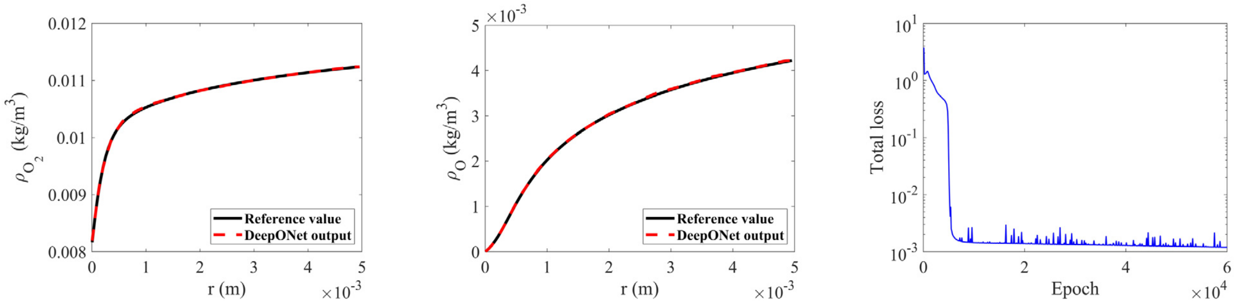

(d) Variable ρ_{O_2} (e) Variable ρ_O (f) Training loss

Fig. 7. Predictions of the series DeepMMNet for the 2T model in the test case with $M_\infty = 13.29$. Only 2 reference data points are known for variables U, T and T_v. The pink circle symbols represent sensor data extracted from the StS calculations (labeled as 'Reference value' in the figure).

4. DeepStSNet framework: architecture and results

The StS simulation can describe the full coupling between vibrational chemical kinetics and fluid dynamics and give detailed vibrational energy distributions. Therefore, in order to predict the quantum state-resolved thermochemical nonequilibrium flowfield from sparse experimental data, the StS variables of the dataset generated in Sec. 2.3 should be used in the above training of DeepONet and DeepMMNet. However, describing the coupled dynamics between StS variables requires too many DeepONets (for predicting densities of vibrational levels $\rho_{O_{2,i}}$, i.e., $G_{\rho_{O_{2,i}}}$), which are very time-consuming to train, especially when rot-vibrational StS [12,26,38] are considered. Moreover, inserting too many DeepONets in the DeepMMNet is detrimental to the stability and convergence of the neural network training. The problem of training DeepONets for all the vibrational levels of O_2 can be alleviated by using the coarse-grained method (CGM) [11,12,26], which is a reduced model for the StS approach.

4.1. Coarse-grained method

We employ the coarse-grained method to reduce the computational expense of the StS approach with an acceptable accuracy. Instead of directly solving the master equations for every vibrational energy level of O_2, we divide these levels into several groups, and the level populations in each group are reconstructed based on the maximum entropy principle [27], which states that molecular collisions like to generate post-collision internal energy distributions that maximize entropy. The strategies for dividing the levels and the reconstruction schemes are detailed in [26,47]. Herein, we use the energy-based grouping strategy [12] by dividing the levels into groups of equal energy intervals. Specifically, the 46 energy levels of O_2 are first divided into 3 groups. The energy width of each group is determined by $\Delta E = \frac{D_0}{N_b}$, where D_0 represents the dissociation energy of O_2 and $N_b = 3$ is the number of groups. As a result, the $0^{th} - 9^{th}$ vibrational levels of O_2 are lumped into the 1^{st} group, the $10^{th} - 20^{th}$ levels are lumped into the 2^{nd} group and the remaining $21^{th} - 45^{th}$ levels are lumped into the 3^{rd} group. Furthermore, the distribution within a group is approximated by a local representation, and the maximum entropy linear model is used for reconstruction, i.e.,

$$\ln n^g_{O_{2,i}} = \alpha^g + \beta^g \varepsilon_i, \tag{13}$$

where g denotes the group and vibrational level $i \in g$. The unknown parameters α^g and β^g in the above formulation are determined by the macroscopic constraints

$$\sum_i n^g_{O_{2,i}} = n^g_{O_2}, \quad \sum_i n^g_{O_{2,i}} \varepsilon_i = E^g_v, \tag{14}$$

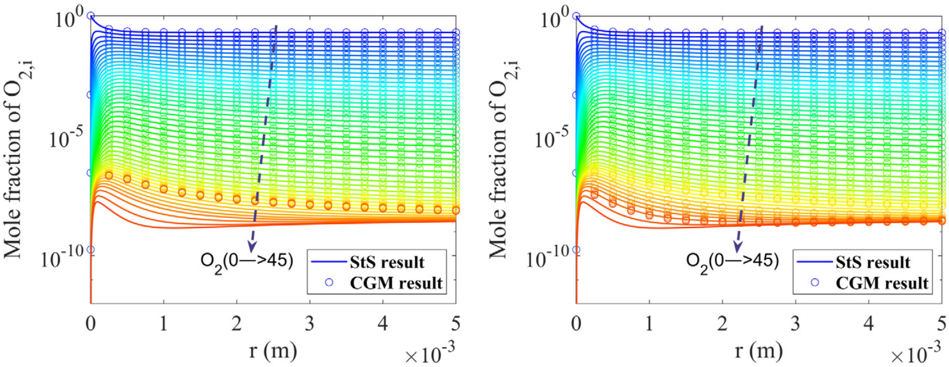

(a) CGM result with 3 groups (b) CGM result with 4 groups

Fig. 8. Mole fractions of $O_2(0-45)$ behind shock wave for the case of $M_\infty = 13.55$. CGM results with 3 groups (a) and 4 groups (b) are given, respectively. And the reference distribution of the StS result is also shown for comparison.

where $n^g_{O_{2,i}}$ and E^g_v are the number density and vibrational energy of group g. Based on the maximum entropy linear model [22,47], the vibrational level distribution within group g can be described by the Boltzmann distribution governed by group vibrational temperature T^g_v (note that in the following, we call T^1_v as T_v for short). The vibrational temperature T^g_v is related to β^g via $\beta^g = -\frac{1}{k_B T^g_v}$ and is calculated by an iterative method from Eqs. (13) and (14).

To test the accuracy of the coarse-grained method, the StS variables of the case with $M_\infty = 13.55$ from the StS dataset are used to generate $n^g_{O_{2,i}}$ and E^g_v. Then the VDF of O_2 is reconstructed from Eqs. (13) and (14). The mole fractions of $O_2(0-45)$ behind shock wave obtained by CGM with 3 groups are shown in Fig. 8(a) for the case of $M_\infty = 13.55$, and the reference distribution of StS results are also shown. The CGM and StS results agree well at low and medium vibrational energy levels. However, CGM results with 3 groups are not satisfactory for describing the distribution of very high vibrational levels (that favor dissociation and become under-population), so significant differences are found between CGM with 3 groups and the StS results. To this end, we make a secondary division for the 3^{rd} group (in 3 groups strategy) to describe better the behavior of the higher vibrational energy levels, i.e., 1^{st} group (0-9), 2^{nd} group (10-20), 3^{rd} group (21-39), and 4^{th} group (40-45). It is seen from Fig. 8(b) that the CGM results obtained with 4 groups capture the behaviors of high energy levels much better than that obtained with 3 groups. It should be noted that the CGM results can be further improved by including more groups, which, however, would take much more time to train the DeepONets. Therefore, CGM results with up to 4 groups are used in the following. Field variables U, T, T_v, $\rho^{i=1,N_b}_{O_2}$ and $E^{i=1,N_b}_v$ (these variables are called 'StS-CGM variables' hereafter) are extracted from the StS variables of the StS dataset. The variable T_v is still needed in the StS-CGM variables because the vibrational temperature is measured in the experiment of Ibraguimova et al. [28].

4.2. DeepONets for the coupled dynamics between StS-CGM variables

We now develop and train DeepONets for learning nonlinear operators to represent the coupled dynamics between StS-CGM variables. We design the following independent DeepONets, describing the coupled dynamics between StS-CGM variables and serving as the building blocks of DeepStSNet:

(i) DeepONets G_U and G_T taking the field variable T_v as the input for the branch net and the velocity U and temperature T as the outputs, respectively (see Fig. 9(a)).
(ii) DeepONets $G^i_{\rho_{O_2}}$ and G_{ρ_O} taking the field variables $[U, T, T_v]$ as the inputs for the branch net and the densities $\rho^i_{O_2}$ and ρ_O as the outputs, respectively (see Fig. 9(b)).
(iii) DeepONets $G^i_{E_v}$ taking the field variables $\left[U, T, \rho^i_{O_2}, \rho_O\right]$ as the inputs for the branch net and the vibrational energy of group E^i_v as the output (see Fig. 9(c)).
(iv) DeepONet G_{T_v} taking the field variables $\left[\rho^1_{O_2}, E^1_v\right]$ as the inputs for the branch net and the vibrational temperature T_v as the output (see Fig. 9(d)).

The above DeepONets are summarized in Table. 2. Again, we take the densities of $\rho^i_{O_2}$ and ρ_O in logscale in the training to improve the accuracy and robustness, and we take the non-dimensionalized data for field variables U, T and T_v and the original data for the vibrational energy of each group E^g_v. The hyper-parameters for these DeepONets are presented in Appendix A. These DeepONets are trained independently by minimizing the MSE loss function. The dataset reported in Sec. 2.3 is again divided into a training, a validation, and a test dataset according to the ratio 0.85: 0.1: 0.05. We have performed sensitivity tests with different training parameters, and the results are similar to the ones obtained by the parameters listed in Appendix A.

Table 2
DeepONets for StS-CGM variables.

DeepONets	Input function	Output function
G_U	T_v	U
G_T	T_v	T
$G^i_{\rho_{O_2}}$	U, T, T_v	$\rho^i_{O_2}$
G_{ρ_O}	U, T, T_v	ρ_O
$G^i_{E_v}$	$U, T, \rho^i_{O_2}, \rho_O$	E^i_v
G_{T_v}	$\rho^1_{O_2}, E^1_v$	T_v

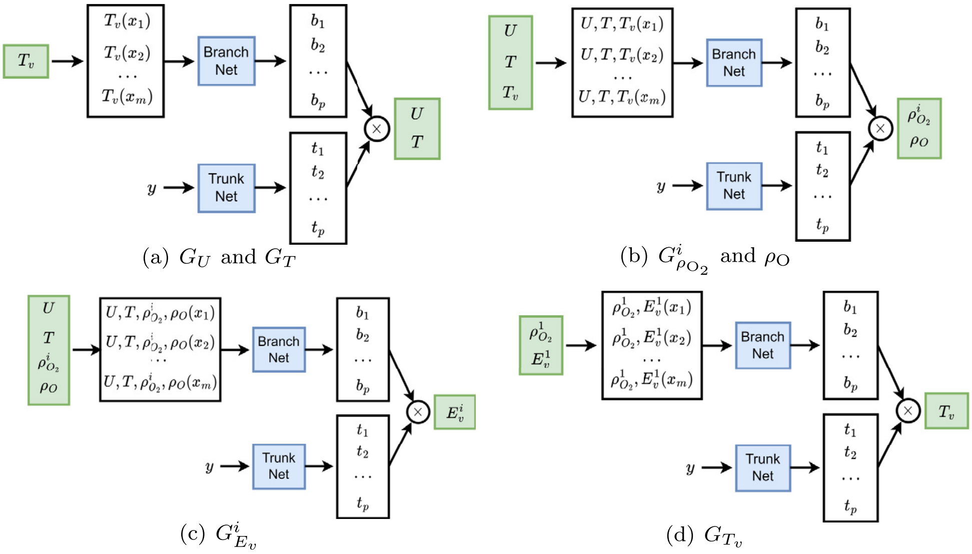

(a) G_U and G_T

(b) $G^i_{\rho_{O_2}}$ and ρ_O

(c) $G^i_{E_v}$

(d) G_{T_v}

Fig. 9. Schematic of DeepONets for the coupled dynamics between StS-CGM variables.

We observe from Fig. 10 that the predictions of DeepONets for the coupled dynamics between StS-CGM (with 4 groups division) variables are in excellent agreement with the StS-CGM variables extracted from reference data obtained in Sec. 2.3. The test samples are randomly chosen from the StS dataset. The corresponding loss functions for training and validation datasets on G_U, G_T and G_{Tv} are also shown in Fig. 10 (a-c), and the trends and orders of magnitude of other variables are similar. Although $\rho^i_{O_2}$ and E^i_v vary by several orders of magnitude downstream of the normal shock, the related DeepONets predict the variation accurately and the MES loss function is the order of 10^{-5}. The DeepONets for StS-CGM variables with 3 groups division are also successfully trained and tested, though the results are not shown here for brevity. The above-trained DeepONets are effective substitutes for solving the StS-CGM governing equations, namely the density and energy of vibrational group (thus VDF of O_2) can be efficiently predicted from macroscopic field variables (U, T and T_v). The present DeepONets serve as building blocks for the design of DeepStSNet for the StS-CGM variables in the following.

4.3. DeepStSNet framework and results

It is intractable to directly measure the distribution of molecular internal energy levels in experimental measurements, which are usually limited to macroscopic field variables like temperature or velocity. Based on the approach of data assimilation used in Secs. 3.2 and 3.3 for the 2T model, a new data assimilation framework, DeepStSNet, for the StS-CGM model is proposed herein and used to predict the quantum state-resolved thermochemical nonequilibrium flowfield from sparse sensor data (experimental measurements).

Since the experiment [28] of interest only gives experimental data of vibrational temperature T_v, a series DeepStSNet (whose schematic is shown in Fig. 11) requiring only a few sensor data of T_v is explicitly designed. A simple NN is trained, which takes the coordinate x as input and outputs vibrational temperature T_v. The data loss ($\mathcal{L}_{\text{data}}$) is calculated as the difference between the NN output and the sensor data. Then, a closed loop of the StS-CGM variables is constructed using the pre-trained DeepONets (reported in Sec. 4.2) embedding the physical constraints. The NN output T_v function is fed into the DeepONets G_U and G_T, which output functions U^* and T^*, respectively. The functions U^* and T^* together with T_v are fed into $G^i_{\rho_{O_2}}$ and G_{ρ_O} to obtain $\rho^{i*}_{O_2}$ and ρ^*_O, respectively. Next, the functions U^*, T^*, $\rho^{i*}_{O_2}$ and ρ^*_O are fed into $G^i_{E_g}$ to predict the energy of vibrational group E^{i*}_v. The output of $G^1_{E_v}$, namely E^{1*}_v, together with the density of first vibrational

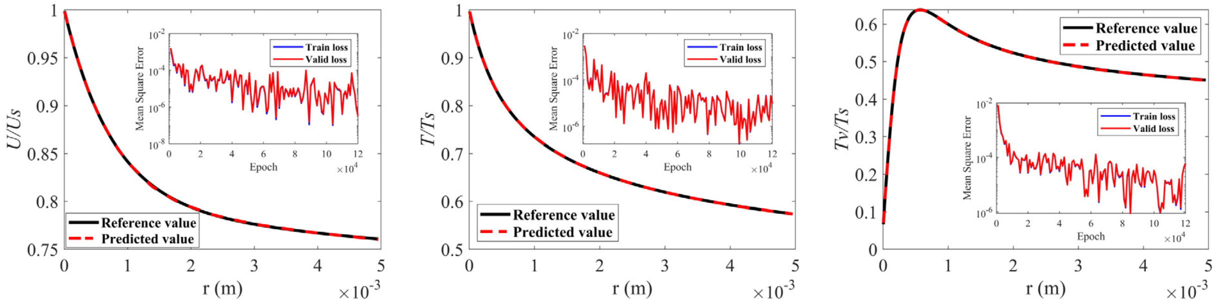

(a) Variable U for $M_\infty = 10.05$ (b) Variable T for $M_\infty = 12.02$ (c) Variable T_v for $M_\infty = 13.33$

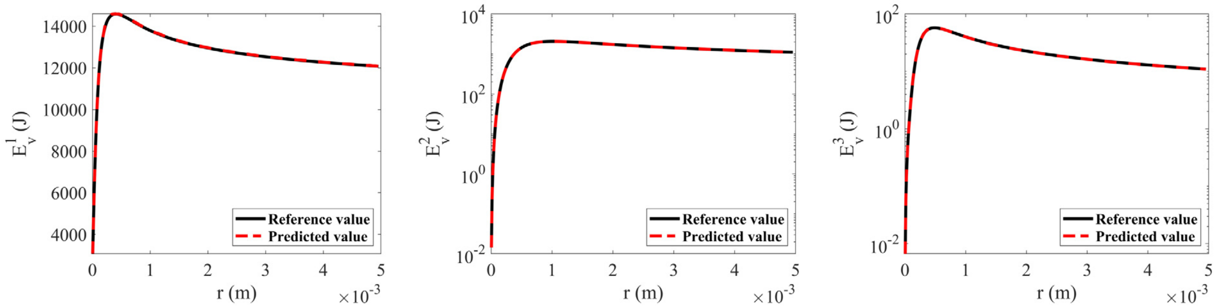

(d) Variable E_v^1 for $M_\infty = 14.78$ (e) Variable E_v^2 for $M_\infty = 11.99$ (f) Variable E_v^3 for $M_\infty = 13.21$

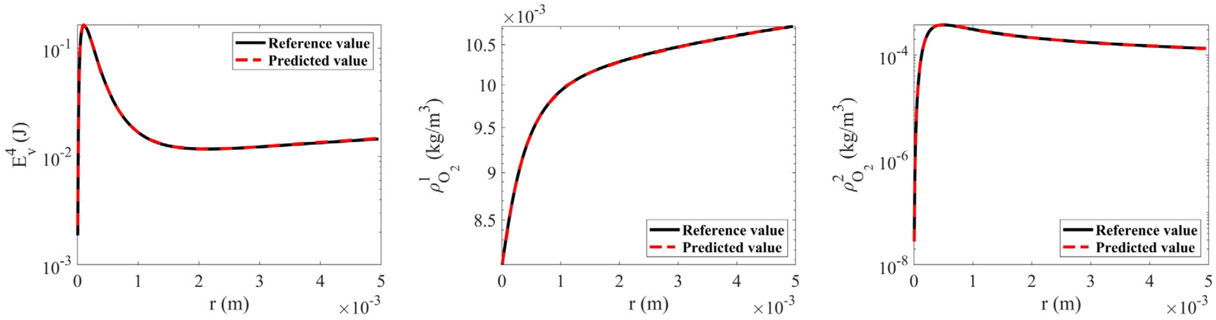

(g) Variable E_v^4 for $M_\infty = 14.53$ (h) Variable $\rho^1_{O_2}$ for $M_\infty = 11.52$ (i) Variable $\rho^2_{O_2}$ for $M_\infty = 13.59$

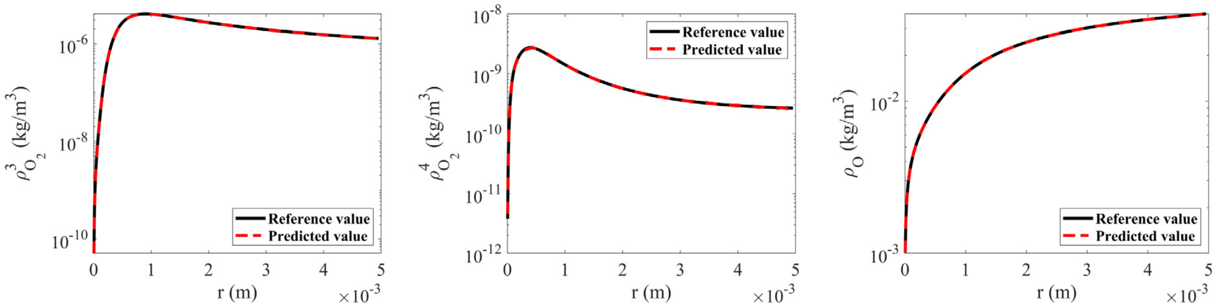

(j) Variable $\rho^3_{O_2}$ for $M_\infty = 12.01$ (k) Variable $\rho^4_{O_2}$ for $M_\infty = 12.53$ (l) Variable ρ_O for $M_\infty = 10.75$

Fig. 10. Predictions of DeepONets for the StS-CGM (with 4 groups division) variables.

group $\rho^{1*}_{O_2}$, are used to predict T_v^* via G_{T_v}. The first operator constraint $\mathcal{L}_{op_1}$ is calculated as the difference between the NN output T_v and the DeepONet G_{T_v} output T_v^*. Since the DeepONet outputs are generally smoother than the NN output in practical training [1], we add second operator constraint $\mathcal{L}_{op_2}$ by differencing the G_{T_v} output T_v^* and the sensor data to make the training more robust. Also, an additional constraint, $\mathcal{L}_G$, related to the global mass conservation is considered by

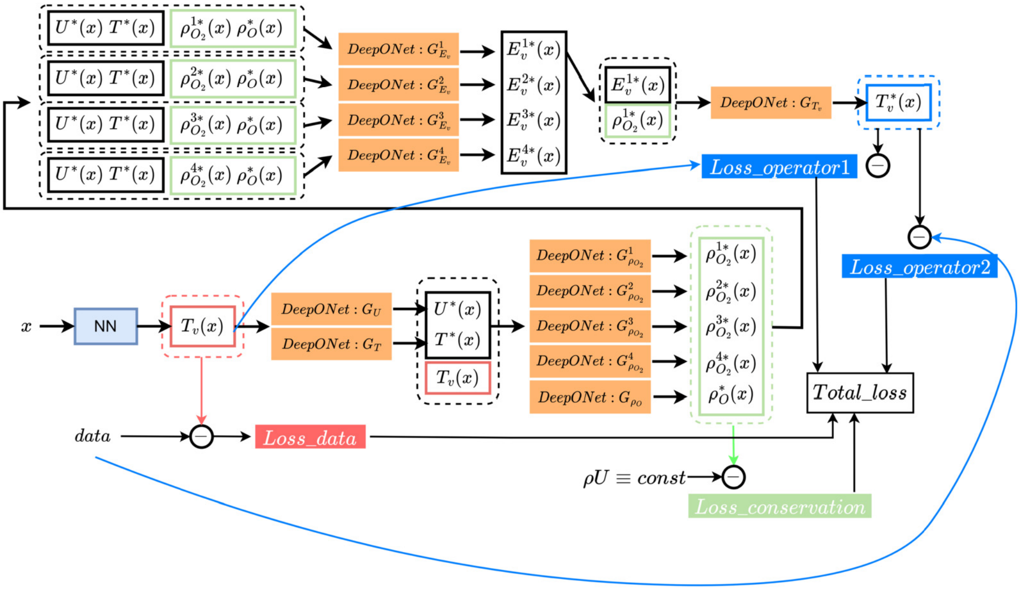

Fig. 11. Schematic of the series DeepStSNet. Sparse sensor data of vibrational temperature T_v are needed.

the difference between the mass flux of the freestream and $(\sum_i \rho^{i*}_{O_2}(x) + \rho^*_O(x))U^*(x)$. As a result, the total loss and the loss terms are represented as follows:

$$\begin{aligned}
&\mathcal{L} = w_{data}\frac{\mathcal{L}_{\text{data}}}{n_d} + w_{op_1}\frac{\mathcal{L}_{op_1}}{n_{op_1}} + w_{op_2}\frac{\mathcal{L}_{op_2}}{n_{op_2}} + w_{reg}\mathcal{L}_{\text{reg}} + w_G\frac{\mathcal{L}_G}{n_G},\\
&\mathcal{L}_{\text{data}} = \sum_{j=1}^{n_d}\left\| {T_v}^j_{\text{data}} - T_v\left(x_j\right)\right\|^2,\\
&\mathcal{L}_{op_1} = \sum_{j=1}^{n_{op_1}}\left\| T_v^*\left(x_j\right) - T_v\left(x_j\right)\right\|^2,\\
&\mathcal{L}_{op_2} = \sum_{j=1}^{n_{op_2}}\left\| T_v^*\left(x_j\right) - {T_v}^j_{\text{data}}\right\|^2,\\
&\mathcal{L}_G = \sum_{j=1}^{n_G}\left\|\rho^*\left(x_j\right)U^*\left(x_j\right) - \text{ Const }\right\|^2.
\end{aligned} \tag{15}$$

To validate the above series DeepStSNet architecture, a test sample with $M_\infty = 13.55$ is selected from the StS dataset, and 5 points of reference data are known for variables T_v. Therefore, $n_d = n_{op_2} = 5$, $n_{op_1} = n_G = 180$. With a large number of pre-tests, we set $w_{data} = w_{op_1} = w_{op_2} = w_G = 1.0$ and $w_{reg} = 1 \times 10^{-5}$ for fast training. The hyperparameters for training the series DeepStSNet are listed in Appendix A.

It is observed in Fig. 12 that the present DeepStSNet results agree well with the reference data of StS calculation. Although only 5 points of T_v data in the flowfield are known, we can still predict the nonequilibrium flowfield details, including the densities and energies of the vibrational groups, thanks to the pre-trained DeepONets, which incorporate the physics laws and the coupled dynamics between the StS-CGM variables. Moreover, the obtained T_v result shows that the NN and DeepONet outputs both match well with the available sensor data.

Furthermore, we investigate the ability of DeepStSNet to predict the flowfield using even fewer sensor data. The same test sample with $M_\infty = 13.55$ is used, and this time only 2 reference data points are known for variables T_v. The training settings are the same as the above ones except for $w_{reg} = 3 \times 10^{-5}$. We observe from Fig. 13 that the DeepStSNet predictions still agree well with reference data even when only 2 data of T_v are available. These results show that one can predict a vibrational-group-resolved flowfield without a large number of data of the field variables by using the present series DeepStSNet.

To obtain the vibrational state-resolved flowfield, the VDF of O_2 are reconstructed from Eqs. (13) and (14). The reconstructed mole fractions of $O_2(0-45)$ behind the normal shock and the reference distribution of StS result are shown in Fig. 8(b). Observe that the excited vibrational levels increase rapidly postshock due to the energy transferred from the trans-

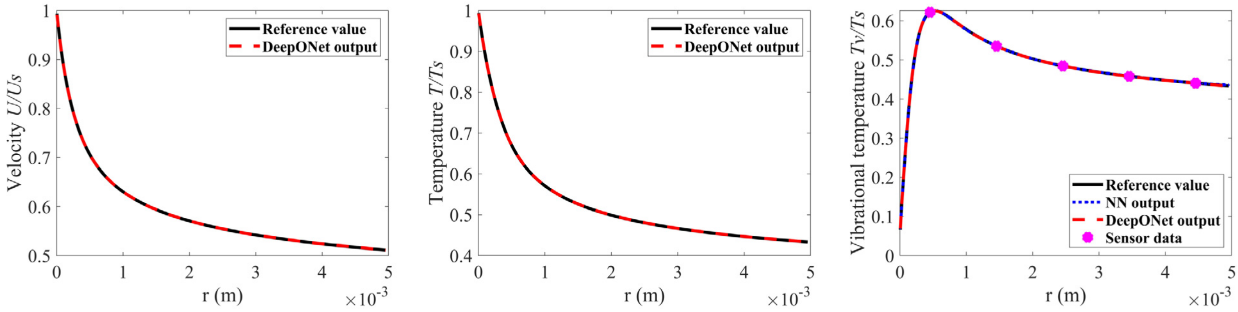

(a) Variable U (b) Variable T (c) Variable T_v

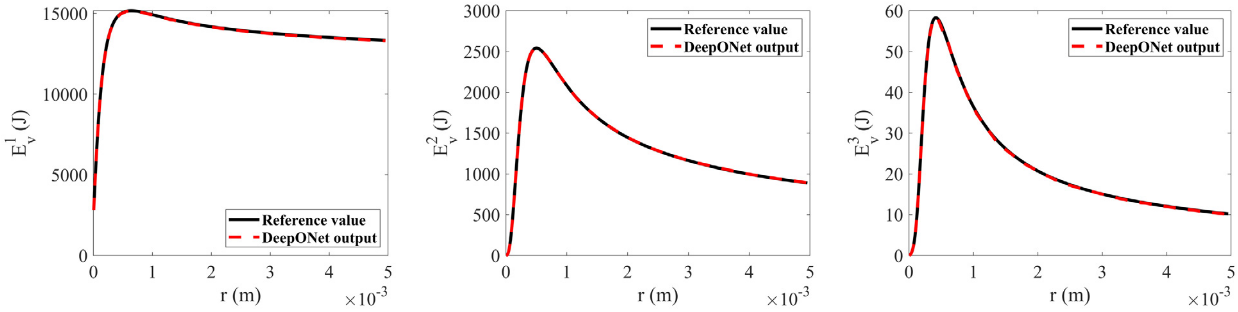

(d) Variable E_g^1 (e) Variable E_g^2 (f) Variable E_g^3

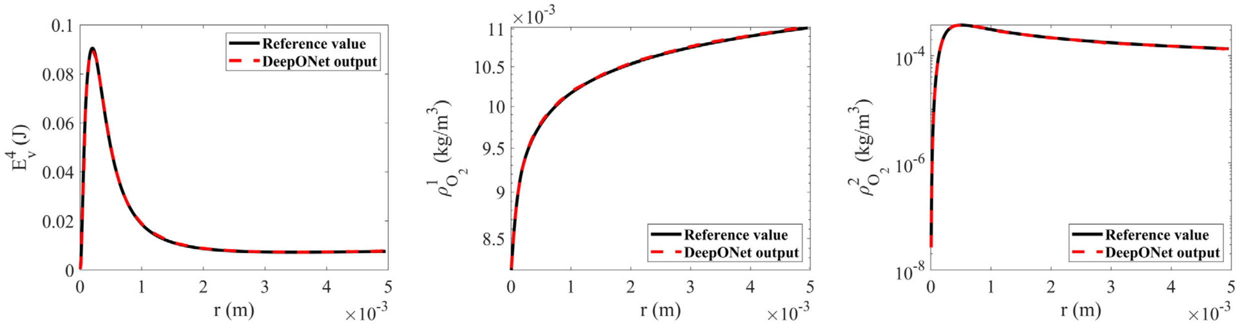

(g) Variable E_g^4 (h) Variable $\rho^1_{O_2}$ (i) Variable $\rho^2_{O_2}$

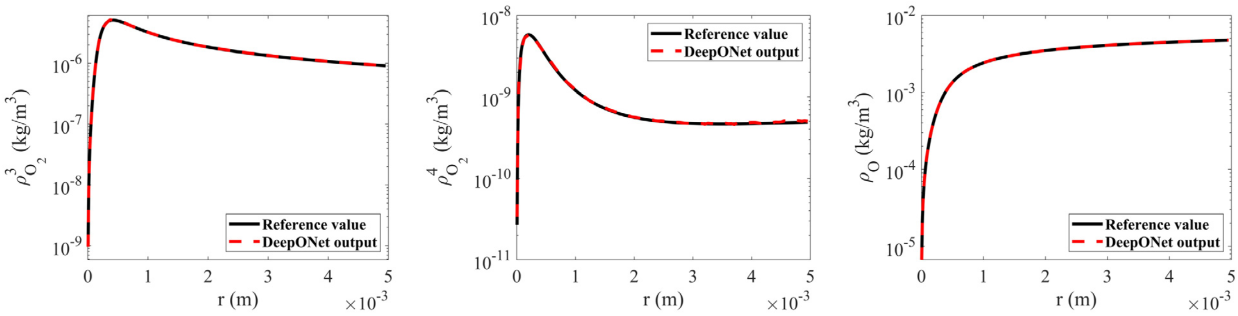

(j) Variable $\rho^3_{O_2}$ (k) Variable $\rho^4_{O_2}$ (l) Variable ρ_O

Fig. 12. Predictions of the series DeepStSNet for the StS-CGM (with 4 groups division) variables in the test case with $M_\infty = 13.55$. The pink circle symbols represent sensor data extracted from the StS calculations (labeled as 'Reference value' in the figure).

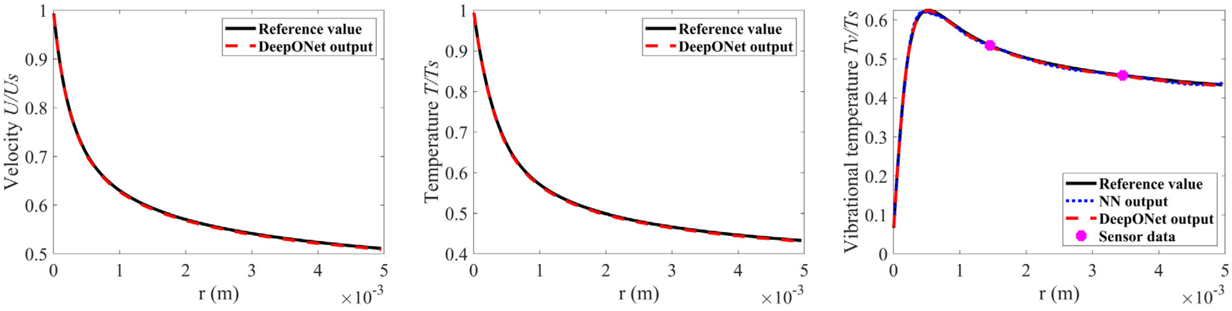

(a) Variable U (b) Variable T (c) Variable T_v

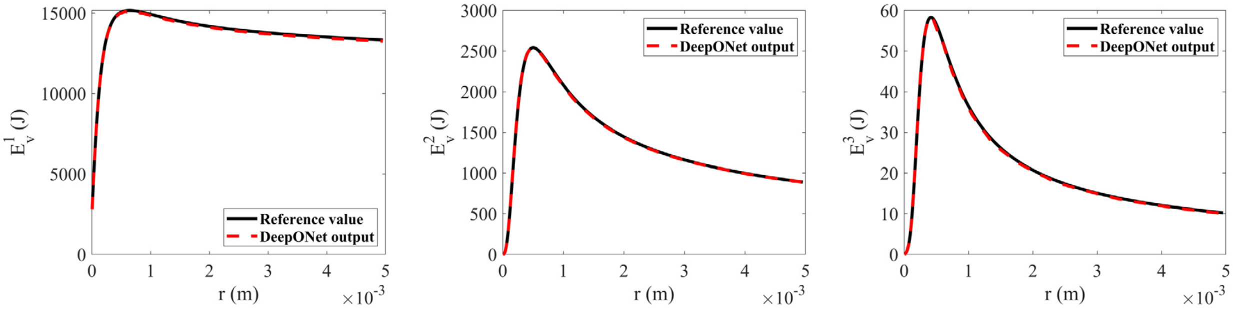

(d) Variable E_g^1 (e) Variable E_g^2 (f) Variable E_g^3

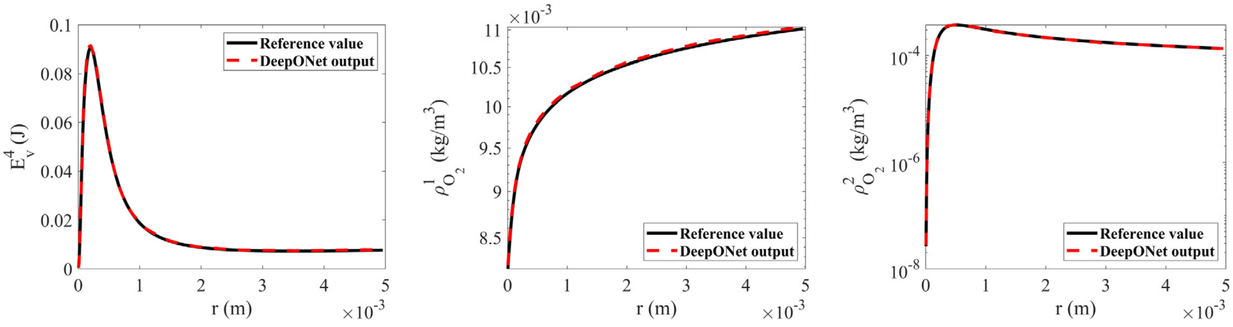

(g) Variable E_g^4 (h) Variable $\rho_{\mathrm{O}_2}^1$ (i) Variable $\rho_{\mathrm{O}_2}^2$

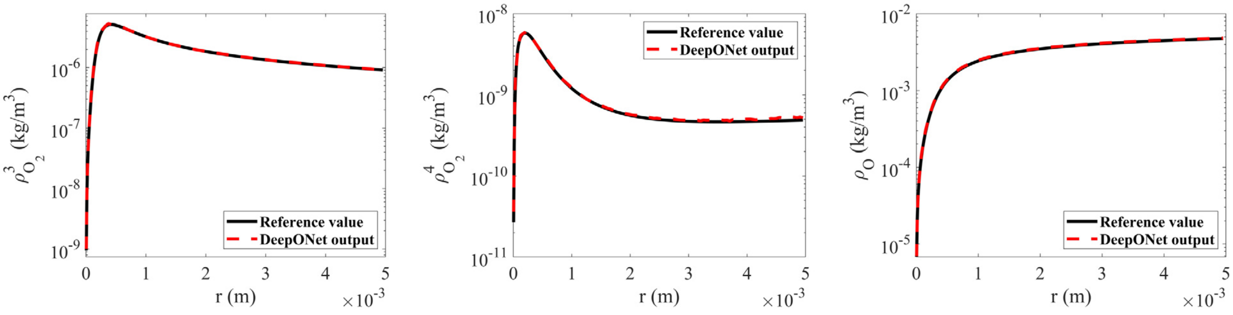

(j) Variable $\rho_{\mathrm{O}_2}^3$ (k) Variable $\rho_{\mathrm{O}_2}^4$ (l) Variable ρ_{O}

Fig. 13. Predictions of the series DeepStSNet for the StS-CGM (with 4 groups division) variables in the test case with $M_\infty = 13.55$. The pink circle symbols (only 2 reference data points are known for variables T_v) represent sensor data extracted from the StS calculations (labeled as 'Reference value' in the figure).

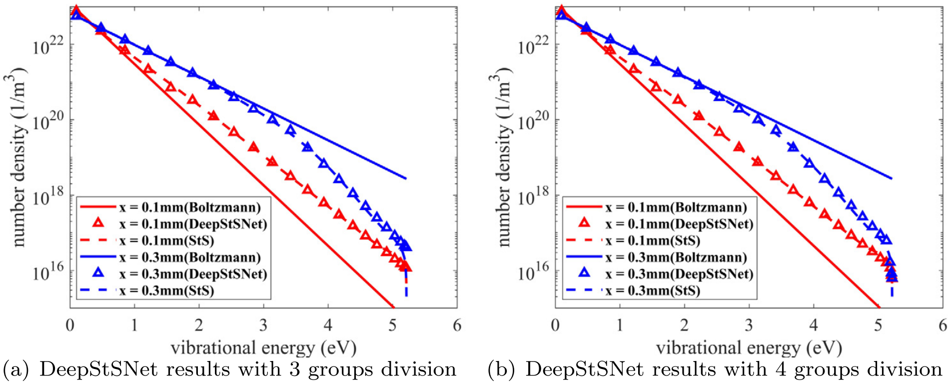

(a) DeepStSNet results with 3 groups division (b) DeepStSNet results with 4 groups division

Fig. 14. Number density distributions of vibrational energy levels of O_2 at selected positions behind the shock for the case of $M_\infty = 13.55$. The DeepStSNet reconstructions with (a) 3 groups division and (b) 4 groups division are compared with the StS results and the local Boltzmann distribution.

lational energy (V–T energy transfer), and then a competition between the V–T energy transfer and vibrationally favored molecular dissociation results in a peak in the mole fraction profiles of the excited vibrational levels. It is also observed from Fig. 8(b) that the DeepStSNet results agree well with the StS results for all the vibrational energy levels except for slight differences of very high levels due to the strong vibration-dissociation coupling effects. And the DeepStSNet results with 4 groups division have overall better performance than the ones with 3 groups division that reported in Fig. 8(a). To check the nonequilibrium deviation, the number densities of vibrational levels of O_2 at two space locations (i.e., 0.1 mm and 0.3 mm) behind the normal shock are plotted in Fig. 14, and the local Boltzmann distribution is also shown for comparison. It is seen that the reconstructed distribution from DeepStSNet results with 4 groups division agrees well with the StS results, even for very high energy levels. At the location of 0.1 mm, the number density of high vibrational levels is significantly larger than the local Boltzmann distribution. This over-population state is because many molecules from low vibrational levels are pumped to high vibrational levels via the V–T processes. As the excited vibrational levels accumulate, the molecular dissociation becomes dominant so that the number density of the excited vibrational levels drops below the local Boltzmann distribution at 0.3 mm. Again, the reconstructed distribution from DeepStSNet results with 3 groups division can not capture the behaviors of very high energy levels compared to StS results. Note that the reconstructed results can always be improved by including more vibrational groups in the coarse-grained treatment, but it will inevitably take much more time to train the related DeepONets and be detrimental to the stability and convergence of the neural network training. In conclusion, the above results demonstrate the ability of the present DeepStSNet framework to reconstruct accurately (compared to reference StS results) the vibrational state-resolved flowfield from sparse sensor data.

5. Reconstruction of state-resolved flowfield with sparse experimental data

Though usually scarce and limited to macroscopic variables, the quantitative experimental data have been used to assess the performance of the 2T model and StS (or StS-CGM) approach [8,13,22]. Nevertheless, the microscopic nonequilibrium distribution of internal energy levels in the flowfield is challenging to measure directly due to the limitations of experimental techniques. Therefore, in this section, we use the DeepStSNet framework proposed in Sec. 4 to assimilate the experiment measurements [28] to predict the vibrational state-resolved thermochemical nonequilibrium flowfield. In the experiment of Ibraguimova et al. [28], the time evolution of vibrational temperature T_v of O_2 behind the normal shock is measured utilizing absorption spectroscopy in the O_2 Schumann-Runge bands. Several sets of measurements are conducted at different operation conditions [28], and only the case with the highest total enthalpy is considered herein, i.e., $V_\infty = 4440$ m/s, $P_\infty = 106.658$ Pa, $T_\infty = 295$ K. Note that the above freestream pressure and temperature are the same as in Table. 1.

The present DeepStSNet framework assimilates experimental data T_v to predict the VDF of O_2 and their confidence intervals related to the inevitable experimental uncertainties (determined by the total error in measuring velocity, initial pressure, absorption value, photomultiplier noise, etc. [28]). Firstly, all the experimental data shown in Fig. 15 are used as sensor data of T_v in training, so $n_d = n_{op_2} = 10$. With a large number of pre-tests, we set the weights of the loss function to be $w_{data} = 1.0$, $w_{op_1} = 3.0$, $w_{op_2} = 5.0$, $w_G = 1.0$, $w_{reg} = 1 \times 10^{-5}$ for stable and fast training. The hyperparameters of the series DeepStSNet are listed in Appendix A. The DeepStSNet predictions are shown in Fig. 15 as the red line (DeepONet output) and light blue dot line (NN output). Both DeepONet and NN outputs of T_v lie within the experimental uncertainty bound, which has a considerable uncertainty about ±500 K. Moreover, the NN output is slightly unsmooth near the first and second experimental data behind the normal shock, which is because these two data points seem noisy and scattered from the others and overfitting occurs in the NN training. On the contrary, DeepONet outputs are always smooth and accurate, even without regularization.

Next, we separate all the experimental data into two-point pairs (a total of $C_{10}^2 = 45$) and assimilate these pairs separately by DeepStSNet to form the equivalent uncertainty bound of DeepStSNet predictions. As reported in Sec. 4.3, two data

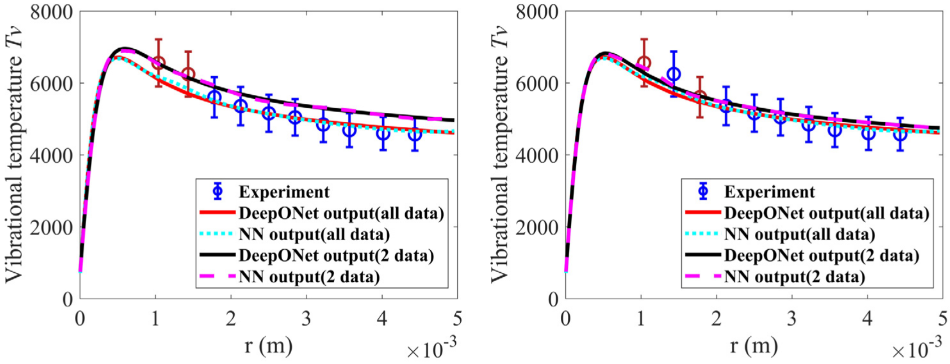

(a) Assimilating 1^{st} and 2^{nd} data points (b) Assimilating 1^{st} and 3^{rd} data points

Fig. 15. The comparisons between experimental measurements and DeepStSNet predictions of vibrational temperature by assimilating (a) the 1^{st}, 2^{nd} experimental data points and (b) the 1^{st}, 3^{rd} experimental data points.

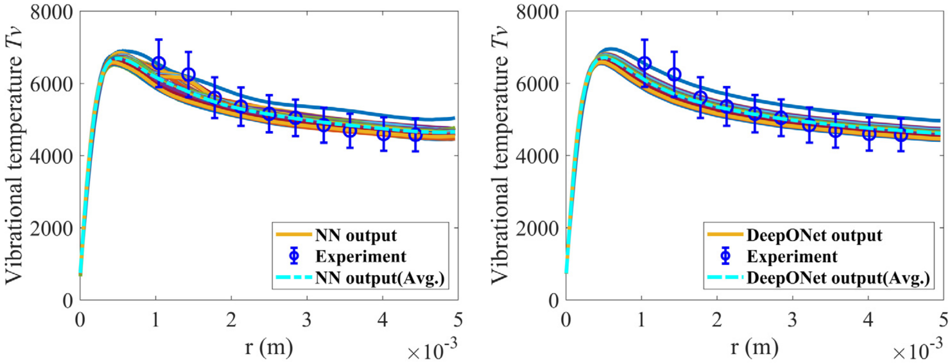

(a) NN outputs (b) DeepONet outputs

Fig. 16. Comparisons of vibrational temperature between experimental measurements and (a) the NN outputs and (b) the DeepONet outputs of DeepStSNet for assimilating 45 two-point data pairs. The averaged results are also shown.

points are sufficient to predict the accurate thermochemical nonequilibrium parameters of the flowfield. Examples of using the 1^{st}, 2^{nd} data points (see Fig. 15(a)) and the 1^{st}, 3^{rd} data points (see Fig. 15(b)) as data constraints of DeepStSNet are performed respectively. It is seen from Fig. 15 that the above results differ from the ones assimilating all the experimental data, which illustrates that the experimental errors make measured data points not rigorously correspond to the same freestream conditions. Furthermore, Fig. 16 gives DeepStSNet predictions of T_v for assimilating all the 45 two-point data pairs. Again, the DeepONet outputs are smoother than the NN outputs. The envelope of DeepONet (or NN) output curves can be considered as the equivalent uncertainty bound of the measured data points, and it nearly overlaps with the error bars estimated from the experimental errors [28], except for the first two data points. By averaging the results for all the data pairs, it is seen from Fig. 16 that the averaged results (dashed lines) lie within the error bars of experimental measurements and are close to the ones assimilating all the experimental data (shown in Fig. 15).

The other ‘StS-CGM variables’ unavailable in the experiment can also be obtained in the series DeepStSNet prediction. Fig. 17 depicts field variables velocity U and translational temperature T, obtained by DeepONets G_U and G_T (shown in Fig. 11) respectively. Again, the curves of assimilating all the 45 two-point data pairs give the uncertainty bound of DeepStSNet predictions, and the averaged results are also shown in the figure. More importantly, the information on vibrational groups is embedded in the DeepStSNet framework. Therefore, the fields of density and energy of the four divided vibrational groups can be predicted by the corresponding DeepONets for each DeepStSNet prediction. By adopting an average operation, Fig. 18(a) shows the averaged densities $\rho^i_{O_2}$ of DeepStSNet predictions. Then the energy-representative vibrational temperature of each vibrational group is calculated by DeepONet $G_{T_{vi}}$ (similar to G_{T_v} and the description of its training is omitted for brevity) based on the averaged results. Finally, the number density distribution of each vibrational energy level is reconstructed from Eqs. (13) and (14) according to the maximum entropy principle and shown in Fig. 18(b). It is noted that the above VDF of O_2 should be considered as the most probable prediction (in the content of the coarse-grained method) from the available experiment measurements of T_v. This most probable prediction of VDF of O_2 shows that the excited vibrational levels are populated significantly due to the V–T energy transfer behind the shock and decreased when dissociation dominates. A piecewise distribution (unsmooth variation of the adjacent levels of two vibrational groups) is seen in the profile of VDF, which is characteristic of the coarse-grained method. Therefore, depending on the accuracy required in

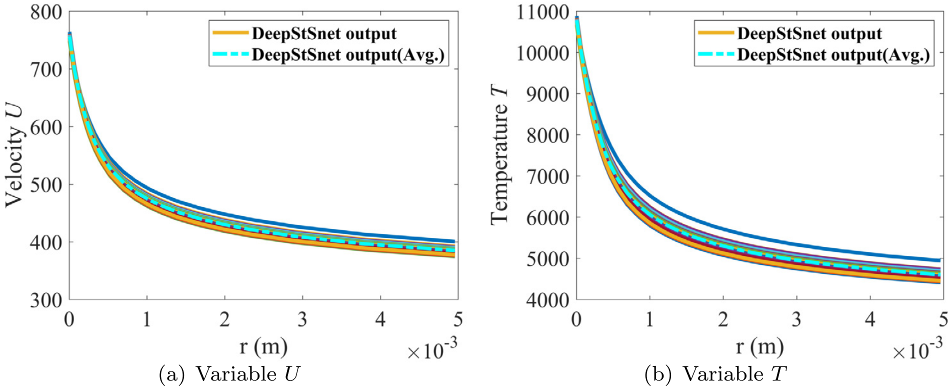

(a) Variable U (b) Variable T

Fig. 17. DeepStSNet predictions of field variables: (a) velocity and (b) temperature.

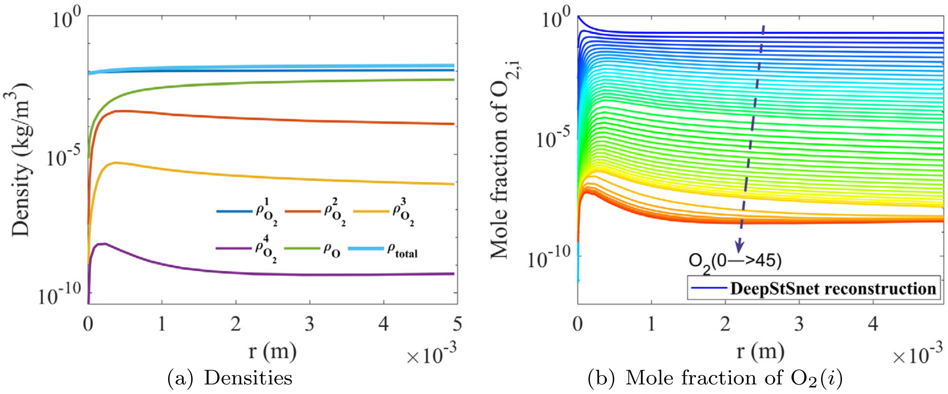

(a) Densities (b) Mole fraction of $O_2(i)$

Fig. 18. Reconstruction of state-resolved flowfield using DeepStSNet framework. (a) Densities of each vibrational group of O_2 and O, and the total density. (b) Mole fraction distribution of $O_2(0 \rightarrow 45)$.

the practical application, a more precise (continuous) prediction of VDF is available if more vibrational groups are divided in the coarse-grained strategy, and it is straightforward to make such an extension in the present DeepStSNet framework.

6. Conclusion

In order to reconstruct the thermochemical nonequilibrium flowfield from scarce experimental measurements, in this work, we first extend the DeepMMNet [1] framework for the 2T model. To obtain the building blocks of the extended DeepMMNet, a series of DeepONets for learning the coupled dynamics between 2T variables are trained and validated. Upon training, these pre-trained DeepONets can predict the target field variables accurately and efficiently. Then the parallel and series DeepMMNet frameworks for the 2T model are designed and proved to perform well in inferring the entire thermochemical nonequilibrium flowfield (on the two-temperature assumption) based on scarce sensor data. Only very few (low to 2) sensor data points are needed to achieve an accurate DeepMMNet prediction thanks to the pre-trained DeepONets and the global mass conservation constraint, which implicitly describes the thermochemical nonequilibrium processes. Moreover, the series architecture only requires sensor data of partial field variables, which is in line with the practical application.

Furthermore, in order to achieve the quantum-state resolution in the reconstruction from scarce experimental data, the DeepStSNet framework is developed based on the StS-CGM model. The coarse-grained method is adopted herein to alleviate the enormous computational cost of the detailed state-to-state approach, and the strategies of dividing the vibrational levels into 3 or 4 vibrational groups are tested and discussed. The pre-trained DeepONets, representing the functional mapping between the StS-CGM variables, are integrated as the building blocks of the DeepStSNet. By testing within the StS reference dataset, the DeepStSNet is proved to reconstruct the vibrational-group-resolved thermochemical nonequilibrium flowfield accurately, and the vibrational state-resolved information is derived via the maximum entropy principle. Then an important step forward is taken to assimilate the experimental data of vibrational temperature from shock tube [28] using the present DeepStSNet. The predicted envelope of vibrational temperature is generated by assimilating all the two-point data pairs, and the averaged result is found to lie within the experimental uncertainty bound. Moreover, the StS-CGM variables unavailable in the experimental measurement, including velocity, translational temperature, and most importantly, density and energy of vibrational groups, are also obtained naturally in the DeepStSNet prediction. Finally, the most probable prediction of the

Table 3
Hyperparameters for the DeepONets (in Secs. 3.1 and 4.2) and neural networks (in Secs. 3.2, 3.3, 4.3 and 5).

	Hidden-layers	Activation function	Optimizer	Learning rate	Epochs
Sec. 3.1	4×100	Adaptive ReLU	Adam	6×10^{-4}	120000
Sec. 3.2	6×50	tanh	Adam	5×10^{-4}	30000
Sec. 3.3	6×50	tanh	Adam	2×10^{-4}	60000
Sec. 4.2	4×128	Adaptive ReLU	Adam	2×10^{-4} for $G^i_{E_v}$ 6×10^{-4} for others	120000
Sec. 4.3	2×100	tanh	Adam	8×10^{-5}	60000
Sec. 5	2×100	tanh	Adam	1×10^{-4}	40000

number density distribution of each vibrational energy level of O_2 is reconstructed. It is thus able to predict the (vibrational) quantum-state information of thermochemical nonequilibrium flowfield based on scarce experimental measurements (of macroscopic field variables) using the present DeepStSNet, and this kind of microscopic reconstruction is beneficial for exploiting the sparse experimental data and uncovering the hidden physicochemical processes in the hypersonic flows. Note that there is no difficulty in extending the present DeepStSNet framework to multicomponent gas flows, like the common five air species O_2/O/N_2/N/NO, which will be reported in a subsequent paper.

CRediT authorship contribution statement

Jiaqi Lv: Methodology, Generating StS data, Investigation, Coding, Writing – original draft, Writing – review & editing, Visualization.

Qizhen Hong: Conceptualization, Methodology, Investigation, Coding, Writing – original draft, Writing – review & editing, Supervision, Project administration, Funding acquisition.

Xiaoyong Wang: Methodology, Coding, Writing – original draft, Writing – review & editing, Visualization.

Zhiping Mao: Conceptualization, Methodology, Investigation, Coding, Writing - original draft, Writing – review & editing, Supervision, Project administration, Funding acquisition.

Quanhua Sun: Conceptualization, Methodology, Writing – original draft, Writing – review & editing, Project administration, Funding acquisition.

Declaration of competing interest

The authors declare that they have no known competing financial interests or personal relationships that could have appeared to influence the work reported in this paper.

Data availability

Data will be made available on request.

Acknowledgement

This work was supported by the National Key R&D Program of China (Grant No. 2022YFA1004500), the Strategic Priority Research Program of Chinese Academy of Sciences (Grant No. XDA17030100), the fellowship of China Postdoctoral Science Foundation through Grant No. 2022M723233 and the National Natural Science Foundation of China (Grant No. 12171404). Q. Hong would like to thank Dr. Sangdi Gu for the helpful discussions.

Appendix A. Hyperparameters of neural networks

To achieve fast and stable training for the DeepONets and neural networks used in the present work, we have performed many (sensitivity) tests with different training hyperparameters to determine the best ones. These hyperparameters are summarized in Table 3. Note that the hidden layers of the branch and trunk nets of DeepONet are set to the same value.

References

[1] Z. Mao, L. Lu, O. Marxen, T.A. Zaki, G.E. Karniadakis, DeepM&Mnet for hypersonics: predicting the coupled flow and finite-rate chemistry behind a normal shock using neural-network approximation of operators, J. Comput. Phys. 447 (2021) 110698.
[2] G.V. Candler, Rate effects in hypersonic flows, Annu. Rev. Fluid Mech. 51 (2019) 379–402.
[3] C. Park, Assessment of two-temperature kinetic model for ionizing air, J. Thermophys. Heat Transf. 3 (1989) 233–244.
[4] C. Park, Nonequilibrium Hypersonic Aerothermodynamics, Wiley, 1990.
[5] P.V. Marrone, C.E. Treanor, Chemical relaxation with preferential dissociation from excited vibrational levels, Phys. Fluids 6 (1963) 1215–1221.
[6] H. Luo, A.A. Alexeenko, S.O. Macheret, Assessment of classical impulsive models of dissociation in thermochemical nonequilibrium, J. Thermophys. Heat Transf. 32 (2018) 861–868.
[7] R.S. Chaudhry, G.V. Candler, Statistical analyses of quasiclassical trajectory data for air dissociation, in: AIAA Scitech 2019 Forum, 2019, p. 0789.

[8] X. Wang, Q. Hong, Y. Hu, Q. Sun, On the accuracy of two-temperature models for hypersonic nonequilibrium flow, Acta Mech. Sin. 39 (2023) 122193.
[9] E. Nagnibeda, E. Kustova, Non-Equilibrium Reacting Gas Flows: Kinetic Theory of Transport and Relaxation Processes, Springer Science & Business Media, 2009.
[10] J. Hao, J. Wang, C. Lee, State-specific simulation of oxygen vibrational excitation and dissociation behind a normal shock, Chem. Phys. Lett. 681 (2017) 69–74.
[11] T.E. Magin, M. Panesi, A. Bourdon, R.L. Jaffe, D.W. Schwenke, Coarse-grain model for internal energy excitation and dissociation of molecular nitrogen, Chem. Phys. 398 (2012) 90–95.
[12] R. Macdonald, R. Jaffe, D. Schwenke, M. Panesi, Construction of a coarse-grain quasi-classical trajectory method I. theory and application to N_2–N_2 system, J. Chem. Phys. 148 (2018) 054309.
[13] L. Campoli, O. Kunova, E. Kustova, M. Melnik, Models validation and code profiling in state-to-state simulations of shock heated air flows, Acta Astronaut. 175 (2020) 493–509.
[14] Q. Hong, X. Wang, Y. Hu, Q. Sun, Development of a stagnation streamline model for thermochemical nonequilibrium flow, Phys. Fluids 32 (2020) 046102.
[15] G. Colonna, F. Bonelli, G. Pascazio, Impact of fundamental molecular kinetics on macroscopic properties of high-enthalpy flows: The case of hypersonic atmospheric entry, Phys. Rev. Fluids 4 (2019) 033404.
[16] I.V. Adamovich, S.O. Macheret, J.W. Rich, C.E. Treanor, Vibrational energy transfer rates using a forced harmonic oscillator model, J. Thermophys. Heat Transf. 12 (1998) 57–65.
[17] M. Lino da Silva, B. Lopez, V. Guerra, J. Loureiro, A multiquantum state-to-state model for the fundamental states of air: the stellar database, ESA SP 714 (2012) 16.
[18] D.G. Truhlar, J.T. Muckerman, Reactive scattering cross sections III: quasiclassical and semiclassical methods, in: Atom-Molecule Collision Theory, Springer, 1979, pp. 505–566.
[19] D. Andrienko, I.D. Boyd, Vibrational relaxation and dissociation in O_2-O mixtures, in: 46th AIAA Thermophysics Conference, 2016, p. 4021.
[20] Q. Hong, Q. Sun, M. Bartolomei, F. Pirani, C. Coletti, Inelastic rate coefficients based on an improved potential energy surface for N_2+N_2 collisions in a wide temperature range, Phys. Chem. Chem. Phys. 22 (2020) 9375–9387.
[21] Q. Hong, M. Bartolomei, F. Pirani, F. Esposito, Q. Sun, C. Coletti, Vibrational deactivation in $O(^3P)$+N_2 collisions: from an old problem towards its solution, Plasma Sources Sci. Technol. 31 (2022) 084008.
[22] J. Hao, C.-Y. Wen, Maximum entropy modeling of oxygen vibrational excitation and dissociation, Phys. Rev. Fluids 4 (2019) 053401.
[23] S. Gu, J. Hao, C.-Y. Wen, On the vibrational state-specific modeling of radiating normal shocks in air, AIAA J. (2022) 1–15.
[24] I. Armenise, E. Kustova, On different contributions to the heat flux and diffusion in non-equilibrium flows, Chem. Phys. 428 (2014) 90–104.
[25] S. Gu, J. Hao, C.-Y. Wen, State-specific study of air in the expansion tunnel nozzle and test section, AIAA J. (2022) 1–15.
[26] M.P. Sharma, Y. Liu, M. Panesi, Coarse-grained modeling of thermochemical nonequilibrium using the multigroup maximum entropy quadratic formulation, Phys. Rev. E 101 (2020) 013307.
[27] R.D. Levine, Molecular Reaction Dynamics, Cambridge University Press, 2009.
[28] L. Ibraguimova, A. Sergievskaya, V.Y. Levashov, O. Shatalov, Y.V. Tunik, I. Zabelinskii, Investigation of oxygen dissociation and vibrational relaxation at temperatures 4000–10800 K, J. Chem. Phys. 139 (2013) 034317.
[29] S.P. Sharma, W. Gillespie, Nonequilibrium and equilibrium shock front radiation measurements, J. Thermophys. Heat Transf. 5 (1991) 257–265.
[30] J. Zhang, W. Ma, Data-driven discovery of governing equations for fluid dynamics based on molecular simulation, J. Fluid Mech. 892 (2020).
[31] C. Ferreira, Gene Expression Programming: Mathematical Modeling by an Artificial Intelligence, vol. 21, Springer, 2006.
[32] A.D. Jagtap, Z. Mao, N. Adams, G.E. Karniadakis, Physics-informed neural networks for inverse problems in supersonic flows, J. Comput. Phys. 466 (2022) 111402.
[33] S. Cai, Z. Wang, L. Lu, T.A. Zaki, G.E. Karniadakis, DeepM&Mnet: Inferring the electroconvection multiphysics fields based on operator approximation by neural networks, J. Comput. Phys. 436 (2021) 110296.
[34] K. Hornik, M. Stinchcombe, H. White, Multilayer feedforward networks are universal approximators, Neural Netw. 2 (1989) 359–366.
[35] T. Chen, H. Chen, Universal approximation to nonlinear operators by neural networks with arbitrary activation functions and its application to dynamical systems, IEEE Trans. Neural Netw. 6 (1995) 911–917.
[36] L. Lu, P. Jin, G. Pang, Z. Zhang, G.E. Karniadakis, Learning nonlinear operators via DeepONet based on the universal approximation theorem of operators, Nat. Mach. Intell. 3 (2021) 218–229.
[37] P. Clark Di Leoni, L. Lu, C. Meneveau, G. Karniadakis, T. Zaki, DeepONet prediction of linear instability waves in high-speed boundary layers, arXiv e-prints, 2021.
[38] M. Sharma Priyadarshini, S. Venturi, M. Panesi, Application of DeepOnet to model inelastic scattering probabilities in air mixtures, in: AIAA Aviation 2021 Forum, 2021, p. 3144.
[39] F. Lordet, J. Méolans, A. Chauvin, R. Brun, Nonequilibrium vibration-dissociation phenomena behind a propagating shock wave: vibrational population calculation, Shock Waves 4 (1995) 299–312.
[40] B. Lopez, M. Lino Da Silva, Non-Boltzmann analysis of hypersonic air re-entry flows, in: 11th AIAA/ASME Joint Thermophysics and Heat Transfer Conference, 2014, p. 2547.
[41] Q. Hong, Q. Sun, F. Pirani, M.A. Valentín-Rodríguez, R. Hernández-Lamoneda, C. Coletti, M.I. Hernández, M. Bartolomei, Energy exchange rate coefficients from vibrational inelastic $O_2(^3\Sigma_g^-)$-$O_2(^3\Sigma_g^-)$ collisions on a new spin-averaged potential energy surface, J. Chem. Phys. 154 (2021) 064304.
[42] F. Esposito, I. Armenise, G. Capitta, M. Capitelli, O–O_2 state-to-state vibrational relaxation and dissociation rates based on quasiclassical calculations, Chem. Phys. 351 (2008) 91–98.
[43] M.L. Da Silva, J. Loureiro, V. Guerra, A multiquantum dataset for vibrational excitation and dissociation in high-temperature O_2–O_2 collisions, Chem. Phys. Lett. 531 (2012) 28–33.
[44] L. Landau, Theory of sound dispersion, Phys. Z. Sowjetunion 10 (1936) 34–43.
[45] S.D. Cohen, A.C. Hindmarsh, P.F. Dubois, CVODE, a stiff/nonstiff ODE solver in C, Comput. Phys. 10 (1996) 138–143.
[46] M. Raissi, P. Perdikaris, G.E. Karniadakis, Physics-informed neural networks: a deep learning framework for solving forward and inverse problems involving nonlinear partial differential equations, J. Comput. Phys. 378 (2019) 686–707.
[47] Y. Liu, M. Panesi, A. Sahai, M. Vinokur, General multi-group macroscopic modeling for thermo-chemical non-equilibrium gas mixtures, J. Chem. Phys. 142 (2015) 134109.